Environmental Fluid Mechanics (2024) 24:1143–1191
https://doi.org/10.1007/s10652-024-10002-4

REVIEW ARTICLES

# River confluences: a review of recent field and numerical studies

George Constantinescu[1] · Carlo Gualtieri[2]

Received: 10 April 2024 / Accepted: 17 July 2024 / Published online: 9 December 2024


## Abstract
Confluences are common components of all riverine systems and are characterized by converging streamlines and potential mixing of separate flows. The fluid dynamics of confluences is characterized by a highly complex structure with several common types of flow features observed. Many theoretical, field, laboratory and numerical studies tried to identify and clarify the main hydrodynamics, morphodynamics and ecological features of river confluences. Those studies spanned a wide range of flow and geometrical conditions ranging from laboratory-scale studies conducted in simplified geometries to field-scale studies of large-scale confluences. In particular, the identification of the main types of coherent structures generated within the post-confluence channel and of their dynamics has led to significant progress in understanding hydrodynamics and mixing processes at natural river confluences. Still, further research is needed to fully clarify how such structures interact among themselves and with the erodible bed and channel banks, how they redistribute momentum and affect transport of heat, suspended sediment, nutrients and what is their role in creating mixing patterns of dissolved and solid matter. In addition, the role of density differences between the incoming waters has garnered increasing attention in confluence studies, while the literature about the relationship between frequently observed species richness and confluence hydrodynamics is still limited. The present paper tries to review the literature on field and numerical studies of natural river confluences with a particular focus on the case in which density contrast affects confluence hydrodynamics and mixing and on large-scale river confluences. The paper discusses some main findings based on the field studies and eddy-resolving numerical simulations conducted by the authors. The application of bioenergetics metric at two large-size concordant bed confluences is also reported. Finally, the paper identifies some directions of future research that should lead to a better understanding of flow structure, transport processes, morphodynamics as well as of the ecological role of river confluences under different conditions.

✉ Carlo Gualtieri
cagualti@unina.it

George Constantinescu
george-constantinescu@uiowa.edu

[1] Department of Civil and Environmental Engineering, IIHR-Hydroscience and Engineering, The University of Iowa, Iowa City, Iowa, USA

[2] Department of Structures for Engineering and Architecture, University of Napoli Federico II, Naples, Italy

**Article highlights**

- Streamwise oriented vortical (SOV) cells that are common at high-angled confluences with negligible density contrast may also form at discordant bed confluences and/or at confluences with moderate density contrast between the tributary flows depending on flow conditions and planform geometry.
- Density contrast between the tributary flows generates new mechanisms for mixing away from the confluence apex. Density contrast generally leads to increased overall mixing, a phenomenon that is independent of the planform geometry and scale of the confluence.
- Sufficiently strong density contrast leads to the fluid from the tributary containing heavier fluid moving beneath the lighter fluid such that, at sufficiently large distances from the confluence apex, the heavier fluid is situated on the opposite side of the post-confluence channel with respect to the tributary containing it before mixing is complete and the fluid in the reach becomes stably stratified.
- Confluence hydrodynamics affects abundance and distribution of aquatic organisms, as well as species richness.

**Keywords** River confluences · Field studies · Numerical studies · Literature review

## 1 Introduction

Confluences are integral and ubiquitous components of all natural drainage networks and riverine systems. Confluences play a critical role in regulating water, sediment, and solutes transport. In addition, confluences are very important in riverine ecology as the tributary can supply supplemental nutrients and energy, which may lead to the development of juxtaposed distinct environments, in terms of water quality, hydraulics and channel morphology [134]. Some organisms may take ecological advantage of the unusual morphology and hydraulics of river confluences (Franks et al., 2002), which, in turn, may affect the bioenergetic features of the flow [55, 58, 59, 111]. The region characterized by converging flow streamlines, enhanced three-dimensionality of the flow, strong redistribution of the streamwise momentum and the presence of large-scale coherent structures generated by the confluence flows is called the *Confluence Hydrodynamic Zone* (CHZ) [71]. This zone generally extends several channel widths downstream of the upstream junction corner. The CHZ generally includes a zone of flow stagnation near the upstream junction corner; an area of flow deflection, also termed collision zone [42], as the tributary enters the confluence,a mixing interface (MI) between the two converging flows; a possible separation zone at the downstream junction corner(s); flow acceleration within the downstream channel; and flow recovery at the downstream end of the CHZ [7]. The current literature on river confluences suggests that the hydrodynamics and morphodynamics within the CHZ are controlled by: (1) the geometry (planform and junction angle) of the confluence, (2) momentum flux ratio of the tributaries, and (3) the level of concordance between the channel beds at the confluence entrance [7, 8, 109]. In addition, the presence of a floodplain in the tributary was found to affect confluence hydrodynamics [91, 92, 174]. Furthermore, differences in the water characteristics (temperature, conductivity, suspended sediment concentration between the incoming tributary flows could affect flow and mixing downstream of the confluence apex due to the difference in the water density of the two incoming streams that induces flow stratification effects (Biron and Lane, 2008 [23],).

During the last three decades, many theoretical, field, laboratory and numerical studies were carried out. Their main goals were to identify and clarify flow hydrodynamics, morphodynamics and ecological processes at river confluences. Those studies spanned a wide range of flow and geometrical conditions, from laboratory-scale to field-scale confluences in large rivers such as the Paranà River [81, 85, 96, 115, 150], the Yarlung Zangbo-Brahmaputra River [171], the Yellow River (Zhang Y. et al., 2015,Zhang T. et al., 2020, the Yangtze River (Jiang et al., 2022; [90–92, 144, 153, 162, 169, 173, 175] and the Amazon River [4, 56, 57, 59, 60, 67, 82, 102, 154]. Studies of natural river confluences involved traditional field investigations [117, 129–131, 146] and numerical investigations (e.g., [19–21, 48, 52, 159, 161, 164]). More advanced techniques based on eddy-resolving numerical simulations were recently used to study the dynamics of the large-scale turbulent structures and mixing [23, 25, 27, 28, 30–33, 42–44, 66],Ismail and Imran, 2022; Jiang et al., 2022). State of the art experimental techniques using a combination of fixed and aerial visual observations [42, 43, 87, 88, 138], and remote sensing imagery [41, 78, 114, 171] were recently used to characterize the dynamics of the mixing interface, the overall mixing between the two streams as well as total suspended sediment (TSS) dynamics and confluence planform evolution. Despite significant progress, several issues need to be further clarified and future research is needed to fully understand hydrodynamics, morphodynamics and ecology at river confluences, to develop generalized theoretical models at such confluences (e.g., following the framework proposed by [149] for cases with negligible density contrast) and to comprehend the effects of confluences on riverine network systems.

The region where two streams come into contact is characterized by the presence of large-scale coherent structures driven by the mean shear and density differences between the two streams and/or the interaction of the separated shear layers forming on the two sides of the confluence apex. This region is referred as the mixing interface (MI). As discussed later, large-scale coherent structures can also form outside the MI and some of these eddies can interact with the MI coherent structures. In the case of confluences for which the level of bed discordance is small, the bulk velocities in the incoming streams are significantly different and the density contrast is relatively small, the MI is in fact a shallow mixing layer. The coherence of the vertically-oriented Kelvin–Helmholtz vortices generated inside the shallow mixing layer decreases with increasing distance from the confluence apex mainly because of dissipation at the bed and vortex stretching. Sufficiently far away from the apex, the shallow mixing layer contains only small-scale turbulent eddies that are the remains of the Kelvin–Helmholtz vortices generated upstream [25]. Some researchers refer to the upstream part of the MI containing vertically-oriented vortices as the shear layer [131, 171] (Fig. 1).

Assuming density contrast effects are relatively mild, several main types of coherent structures were found to play a critical role for mixing and transport of pollutants, suspended load, and bedload downstream of the confluence apex. The first type is associated with vertically oriented vortices (VOVs) inside the MI. These vortices can be easily observed looking at the free surface if the turbidity or color of the two streams is different. The second type is represented by fairly circular, highly coherent streamwise orientated vortices (SOVs) forming in the immediate vicinity of the MI at angled confluences. The SOV cells are not MI coherent structures though the presence of a MI is required for them to form. The SOV cells are generally not visible looking at the free surface. These vortices should not be mistaken with the larger-scale secondary flow cells that can be generated in the downstream channel on one or both sides of the MI especially if the channel

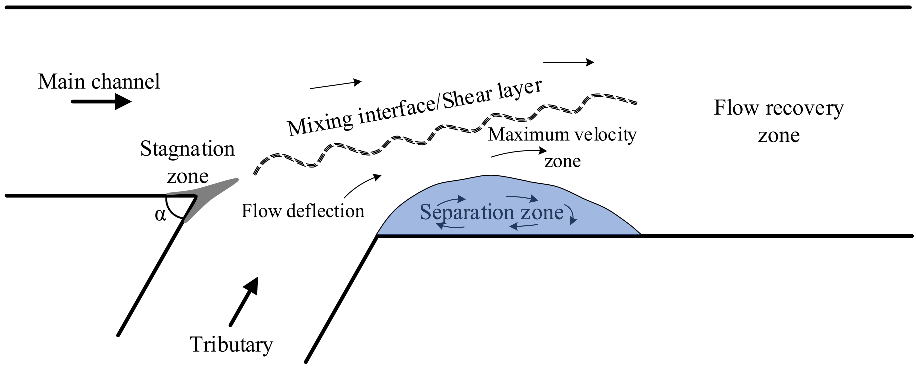


**Fig. 1** Flow patterns at an asymmetrical confluence. Reproduced from Yuan et al. [177]

curvature is strong or with near-bank cells induced by turbulence anisotropy, generally referred as Prandtl's second kind secondary currents. Meanwhile, the secondary flow cells can act toward increasing or decreasing the coherence of the SOV cells depending on their sense of rotation relative to the one inside the SOV cells. Finally, large-scale particle image velocimetry (LSPIV) observations [138] have shown that the MI can be subject to episodic aperiodic pulses where its position becomes strongly disturbed for some time before recovering back to a quasi-equilibrium state. This phenomenon is not yet fully explained but likely due to unsteadiness in the water-surface pressure-gradient field as the flows compete for space within the confluence.

Vertically orientated vortices (VOVs) have been observed in numerous laboratory, field and numerical studies (Biron et al., 2019; [25, 27, 29–33, 39, 86–88, 119],Rogers and Moser, 1992; [130, 138, 146]). Constantinescu et al. (30, 31) identified two different mechanisms that result in generation of VOVs with different physics (Fig. 2). If the velocity and momentum ratios between the merging rivers are close to unity, the stagnation region at the junction corner behaves similarly to a turbulent wake developing in the lee of bluff bodies. Downstream of the stagnation region, the interaction between the separated shear layers forming on the two side of the confluence apex results in the generation of counter-rotating vortices inside the MI (*wake-like* mode). The coherence of these vortices is a function of the bathymetry close to the confluence apex. Often a strong wake-like mode occurs when the size of the stagnation region is relatively large such that the interaction between the eddies shed in the two separated shear layers can result in the formation of relatively large vortices. If the velocity ratio or the momentum ratio is much larger than unity, the MI can be described as a shallow mixing layer in which co-rotating vortices are generated via the Kelvin–Helmholtz instability driven by the inflection point in the mean velocity profile across the MI. As they are advected inside the MI, these vortices undergo vortex pairing which is the main mechanism for the growth of the thickness of the MI. As a result of vortex pairing, these vortices can attain sizes that are much larger than the channel flow depth [30, 31]. Flow shallowness effects become important at large distances from the confluence apex where vortex pairing ceases and these vortices are stretched and eventually lose their coherence [25, 27]. Hence, in such MIs the VOVs are quasi to-dimensional, and co-rotating (Kelvin–Helmholtz mode). At natural river confluences where the momentum and velocity ratios of the incoming flows are close to one, both modes can be present with the wake-like mode being dominant close to the confluence apex and the Kelvin–Helmholtz mode being

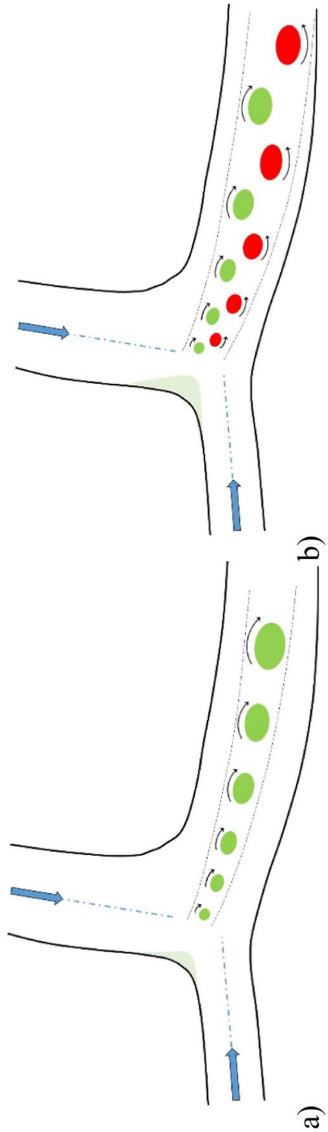


**Fig. 2** Sketch showing the structure of the mixing interface (MI) in the: **a** Kelvin–Helmholtz mode. The MI contains co-rotating vortices; **b** Wake-like mode. The MI contains counter-rotating vortices and the wake region at the confluence apex is relatively large. Reproduced from Cheng and Constantinescu [23]

dominant further downstream where the channel bathymetry and spanwise distribution of bed roughness may create appropriate conditions for the emergence of a conventional shallow mixing layer Recent studies have proposed an intermodal behavior of mixing at angled confluences. Sukhodolov et al. [149] showed that although the momentum flux ratio is not unity the wake-like mode is dominant at short distances from the stagnation zone, while the Kelvin–Helmholtz mode becomes dominant farther downstream.

The mechanism for the formation of SOV cells in the immediate vicinity of the MI and their role in the formation of the confluence scour hole were first described by Paola (1997). Direct evidence of their existence and a detailed description of their dynamics and role in mixing and sediment entrainment were possible via eddy resolving simulations [27, 30, 31, 33]. Such vortices were also the focus of several recent experimental investigations [43, 148],Duguay et al., 2023). SOV cells form due to loss of transverse momentum as two streams with different orientations come into contact at angled confluences (e.g., at confluences with a large angle between the two tributaries). As the kinetic energy is converted into potential energy, the free surface elevation increases near the part of the MI where the cores of the two streams come into contact. In turn, this superelevation induces a secondary flow directed from the free surface toward the bed and then away from the centerline of the MI. This secondary flow eventually raised back toward the free surface and generates SOV cells in the immediate vicinity of the MI [27, 28, 30, 66, 148]. This also explains why the SOV cells forming on the two sides of the MI have an opposite sense of rotation. Multiple, co-rotating SOV cells can form on one or both sides of the MI (Cheng and Constantinescu, 2012, 2021). At asymmetrical confluences, the SOV cells on the tributary side are generally more coherent [23]. The formation mechanism of SOV cells is totally independent of the presence of density contrast between the two tributaries, but density contrast can act toward weakening or suppressing them.

Oblong-shaped helical (secondary flow) cells are also a common feature of the flow inside the CHZ at river confluences where they occupy a significant part of the cross section on one or both sides of the MI. They are mainly caused by upstream secondary circulation in the merging rivers and planform post-confluence channel curvature [1, 3],Bradbook et al., 2000; [42, 66, 70, 76, 109],Paola, 1977; [127–129],Rhoads and Johnson, 2018; Riley and Rhoads, 2012; Riley et al., 2015; [146–148, 169]. In the case of field studies, it was argued that their contribution might be overstated by the processing method of the acoustic velocimetry data [80].

It is not always easy to distinguish between helical cells and SOV cells as they are both oriented along the streamwise direction. One important difference is that helical cells are scaling with the tributaries channel width so their aspect ratio in a cross section is much larger than one, while SOV cells are close to circular and scale with the local flow depth [42, 66]. Furthermore, it is expected that those mentioned classes of coherent structures should interact across the MI leading to the complex hydrodynamic patterns observed at river confluences with natural bathymetry. A further source of large-scale vorticity was found to be flow separation over the scour hole's avalanche faces [8, 9],Biron and Lane, 2008; [42].

Buoyancy effects associated with strong density difference between the merging rivers were found to generate a spatially-developing lock-exchange-like flow [11, 26, 28, 33, 43, 44, 57, 65, 66, 69],Ismail and Imran, 2022; Jiang et al., 2022; [81, 86, 97],Ramón et al., 2013, 2014, 2016; [158]. For such cases, the coherence of the VOV vortices is rapidly lost away from the confluence apex due to stretching associated with the formation of a near-bed intrusion of heavier fluid and of a free-surface intrusion of lighter fluid 'advancing' in opposite directions with increasing distance from the confluence apex. The instantaneous flow fields contain streamwise-oriented cells along the interface separating the regions containing heavier and lighter fluids [28, 66]. These cells should not be mistaken with the aforementioned, classical SOV cells as their formation mechanism is in fact similar to the interfacial Kelvin–Helmholtz vortices forming in a temporally-evolving lock-exchange flow.

Finally, river confluences also have important ecological [134] and morphological functions [10], and recent research is exploring how hydrodynamics might explain ecological richness about confluences. Understanding the potential effects of confluences on riverine ecology is important for the development of local and basin-scale management strategies [107, 133, 134]. Benda et al. [5] presented a network dynamics framework indicating the ecological importance of riverine confluences. Geomorphological adjustments, biological diversity and consequent changes in the physical heterogeneity of confluences are significant [5, 126, 133]. The confluence region increases productivity of supplemental nutrients [46] and adjusts the thermal regime (Milner and Petts, 1994). This region is also characterized by a juxtaposition of distinct tributary environments that enhance particular ecological processes such as channel morphology [120] and refugia [49, 133]. Some studies have demonstrated that species richness peaks just downstream of the river confluence [45, 46, 75, 103, 111]. Other investigations focused on processes taking place across the environmental interfaces [37] of the channel, such as the factors affecting the distribution of total dissolved gas at a confluence [141] and its effect on fish ecology [140], the atmospheric reaeration at a confluence [54, 143, 177], and large wood transport [176]. Confluence geometry, hydrodynamics, and morphodynamics were also found to significantly affect hyporheic exchange rate and patterns. Information on hyporheic fluxes at river confluences can be found in the studies conducted by Cheng et al. [24], Lambs [79], Martone et al. (104, 105, 106) and Song et al. [145]. In addition, entropy-based methods were applied to predict discharge and velocity profiles at confluences [4, 175] and to investigate bedforms characteristics at a confluence in the Amazon Basin (Gualtieri, 2020b). Finally, water chemistry and quality, and the transport and mixing of contaminants at a river confluence were studied using laboratory and field measurements and numerical simulations [16, 94],McKay, 1970; [113, 125, 168]. However, the relationship between the observed species abundance and richness and confluence hydrodynamics is not yet well understood. Though several studies of ecological processes at river confluences are available [15, 17, 40, 55, 58, 155, 172, 173], this research field is in its infancy given the complexity and inherently multidisciplinary nature of the topic.

The main goal of the present paper is to present and discuss some recent advancements, as well as current research topics, in both field and numerical studies of natural stream confluences with a particular focus on the case in which density contrast effects are sufficiently large to affect confluence hydrodynamics, turbulence and mixing. A particular focus is on explaining the mechanisms that control thermal mixing at large-scale river confluences. The examples used to illustrate the dynamics of coherent structures, their roles in mixing and different mechanisms are mostly based on previous work conducted by the authors and their collaborators. In particular, the paper tries to highlight the critical role played by large-scale turbulence in mixing and sediment entrainment inside the post confluence channel. Section 2 presents the main methodologies used in numerical and field studies of river confluences. Then, the dynamics and role of large-scale coherent structures at concordant bed confluences with negligible density contrast are presented and discussed in Sect. 3. This case can be considered as a 'simple' or 'canonical' case in terms of natural river confluences with respect to which additional flow and/or geometrical 'complications' may be present. Sections 4 and 5 consider two such 'complications' associated with increasing stratification effects due to density contrast between the incoming streams and with the presence of a large bed discordance in cases where a small tributary joins a large river, respectively. In Sect. 6, some main results exemplifying the relationship between confluence ecology and hydrodynamics are reviewed and the application of bioenergetics metrics at two large-size concordant bed confluences is presented and discussed. Finally, Sect. 7 reviews some recent applications of remotely sensed image-based techniques and methods to river confluences to stress the large potential they have in the identification of planform evolution and mixing patterns. The paper concludes with a discussion of research needs and challenges, and proposes some directions for future research that, in the opinion of the authors, may lead to significant advancements in understanding the physics of these flows, the ecological functions of natural stream confluences and in formulating a theoretical framework that can be used to make engineering predictions.

## 2 Main methodologies applied in numerical and experimental studies about river confluences

### 2.1 Numerical simulations

The numerical results discussed in the paper were obtained by performing fully three-dimensional, high-resolution Detached Eddy Simulations (DES) which allow capturing the energetically-important coherent structures generated inside the post-confluence channel and their dynamics, a detailed description of the secondary flow, as well as evaluating the bed shear stresses and quantifying the effect of the presence of coherent structures near the bed surface on the bed shear stress distributions. The nondimensionalized Navier Stokes equations are expressed in generalized curvilinear coordinates and integrated in time using an implicit fractional-step method combined with a double time step algorithm. The Boussinesq approximation is used to account for the effects of the (non-uniform) density on the velocity field. An advection–diffusion equation is solved for the nondimensional density/temperature, C. A slip (zero shear stress) boundary condition is imposed at the free surface. Precursor eddy-resolving simulations are conducted to generate the instantaneous velocity fields (fully developed channel flow) that are then specified at the inlet sections of the two tributary channels in the main simulations. The lateral walls and bed surfaces are generally treated as no-slip, rough surfaces with a prescribed value of the average bed roughness. A convective boundary condition [136] is used at the exit boundary in the post-confluence channel. The values of the variable C at the two inlets are specified as 0 or 1 corresponding to the high and low temperature streams. On the other surfaces, the gradient of C in the direction perpendicular to the surface is set equal to zero (zero flux condition).

Details of the numerical method employed by the viscous flow solver are given in Chang et al. (2007) and Constantinescu et al., [30]. The detached eddy simulations were performed using the Spalart–Allmaras turbulence model as the base RANS model. By modifying the turbulence length scale definition, the Spalart–Allmaras turbulence model starts behaving like an LES model away from the solid boundaries. The governing equations and details on the implementation of rough-bed boundary conditions can be found in Keylock et al., [73] and Zeng et al. [179]. Grid points are clustered near the solid boundaries (e.g., channel bottom, confluence apex, channel banks) to resolve the attached boundary layers and inside the MI region.

The DES solver was validated for several important types of simpler flows that are encountered at river confluences. They include flow in curved open channels with complex bathymetry (e.g., see [178],Koken et al., 2013) and shallow mixing layers forming between parallel streams in constant-depth channels [25]. DES accurately predicted the vortical structure and spatial development of the shallow mixing layer including the streamwise variations of the lateral shift of its centerline and its width and the frequency of passage of the Kelvin–Helmholtz billows [25]. The scalar transport module was validated by Chang et al. (2007). Validation simulations for natural river confluences are discussed by Constantinescu et al. (30, 31, 33). DES accurately predicted the mean velocity, turbulent kinetic energy and mean temperature distribution inside the CHZ of the confluence between the Kaskaskia River (KR) and Copper Slough (CS) stream (defined as KRCS) based on comparison with the field data of Sukhodolov and Rhoads [146] and Rhoads and Sukhodolov [129]. Moreover, the accuracy of the time-averaged quantities and turbulence statistics obtained from the DES data was found to be higher than that of the RANS simulations performed using the same grids.

### 2.2 Field studies

The acoustic Doppler current profiler (ADCP) is the standard instrumentation used for hydrodynamic field studies. ADCPs can be used either from moving or fixed vessels to measure the flow field and to identify the riverbed location. ADCPs can also be used to measure water temperature near the surface and backscatter intensity which, after proper calibration, can be related to suspended sediment concentration [150, 151]. Measurements performed from boats moving across river transects are capable to efficiently measure the flow discharge with an acceptable accuracy and to identify the three-dimensional flow field characteristics such as large secondary flow cells. Fixed vessel applications aim at investigating turbulence at some points of the domain. In addition, in field studies, the morphological structures of the channel can be investigated using high-resolution acoustic and seismic methods, such as echo-sounding and sub-bottom profiling [67]. Finally, water chemistry and quality parameters, such as local temperature, pH, conductivity, turbidity and total suspended sediment (TSS) concentration can be measured with water sampling, while vertical profiles of those parameters can be obtained using a multi-parameter probe.

## 3 Large scale coherent structures at concordant bed confluences: effect on mixing

### 3.1 Mixing interface dynamics

Numerical simulations performed for the KRCS confluence (Illinois, USA) are used to illustrate how changes in the momentum ratio and planform geometry affect the structure of the MI [30–33]. The KRCS confluence (Fig. 3a) is an asymmetric, concordant bed confluence with the CS tributary oriented at an angle $\alpha_2 = 60°$ relative to the centerline of the post-confluence channel and the KR tributary fairly well aligned with the post-confluence channel ($\alpha_1 \approx 0°$). The average flow depth in the post-confluence channel, D, is about 0.3–0.4 m, the Reynolds number defined with D and the average bulk velocity in the two tributaries is of the order of $10^5$ and the channel Froude number is less than 0.3. A large, elongated confluence hole with a maximum flow depth of

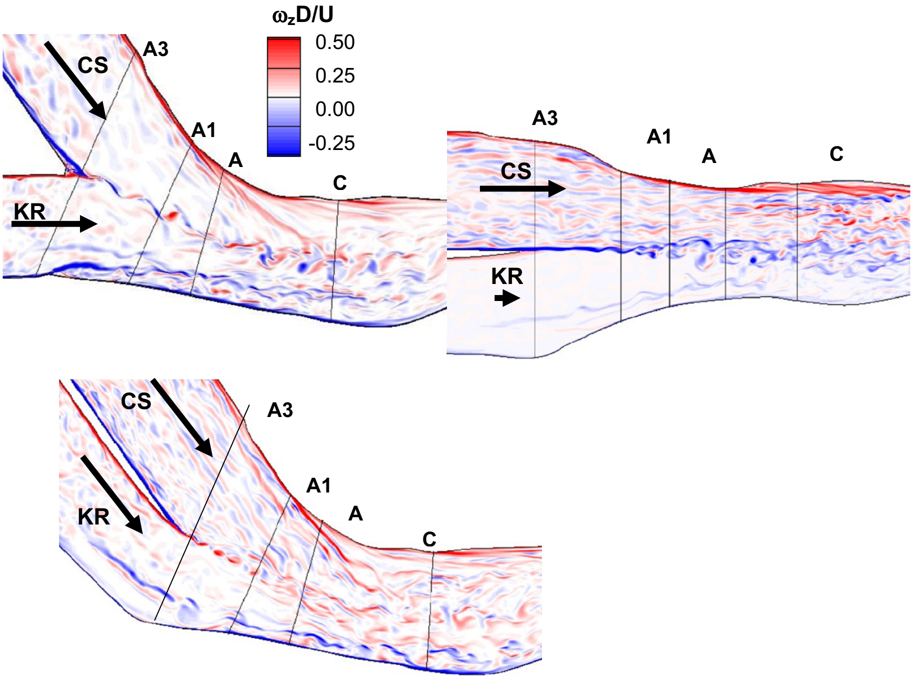


**Fig. 3** KRCS simulations with no density difference between the two streams. Distribution of the vertical vorticity, $\omega_z D/U$, in the instantaneous flow in a horizontal surface situated 0.1D below the free surface. **a** Case 1 (VR≈1, $\alpha_1 = 0°$; $\alpha_2 = 60°$); **b** Case 2 (VR = 4.1, $\alpha_1 = 0°$; $\alpha_2 = 0°$); c) Case 3 (VR≈1, $\alpha_1 = 60°$; $\alpha_2 = 60°$). Reproduced from Constantinescu et al. [32]

about 3D is present downstream of the apex. It extends between sections A1 and A. The average bed roughness height is 0.01 m. With changing hydrograph, the momentum ratio (MR) and velocity ratio (VR) at this confluence are highly variable. Results are discussed for two cases with VR≈1 and VR = 4.1 corresponding to a larger velocity in the CS tributary. The simulations discussed in this section were performed with a bulk Richardson number, $Ri = g\rho_1 - \rho_2\left(D/U^2\right)$ of zero (no density contrast between the incoming streams) corresponding to field cases in which the difference between the temperatures of the two tributaries are less than 1°Csuch that stratification effects due to nonuniform temperature can be neglected [66]. In the definition of the bulk Richardson number, the densities of the two streams are $\rho_1$ and $\rho_2$, g is the gravitational acceleration, $D$ is the average flow depth in the CHZ downstream of the confluence apex, and U is the mean velocity inside the CHZ that is often approximated as the average bulk velocity in the two tributaries.

To exemplify and better understand the conditions that lead to the Kelvin–Helmholtz mode or the wake-like mode being dominant inside the MI, the planform geometry of the KRCS confluence (see Case 1 in Fig. 3a) was modified and additional simulations were conducted with the CS tributary being close to parallel to the post-confluence channel (Case 2, $\alpha_1 = 0°$; $\alpha_2 = 0°$, Fig. 3b) and with the KR tributary rotated such that it becomes parallel to the CS tributary (Case 3, $\alpha_1 = 60°$; $\alpha_2 = 60°$, Fig. 3c). Both VR and MR were close to unity in Case 1 and Case 3. Case 2 was conducted with a larger velocity in the CS stream such that VR = 4.1. Except for the rotation of the tributary channels, the bathymetry was the same in the three cases.

Simulation results for Case 1 show that the MI position follows approximatively the centerline of the post-confluence channel and the mean velocity ratio across the MI remains close to one at most streamwise locations downstream of the confluence apex (Constantinescu et al., 2010). As a result, one expects the wake-like mode to dominate not only close to the confluence apex but also further downstream inside the CHZ and the MI to contain counter-rotating VOVs, as shown in the sketch in Fig. 2b. The instantaneous fields of the vertical vorticity at the free surface in Fig. 3a show the formation of elongated patches of negative and positive vorticity close to the confluence apex corresponding to the VOVs in their incipient formation phase. As they are advected downstream, the shapes of these vorticity patches become more circular. No merging occurs between these patches as they are advected inside the MI.

In Case 2 the confluence angle is close to zero and VR > > 1 at all streamwise locations inside the CHZ. Similar to Case 1, the MI remain close to the centerline of the post-confluence channel. The MI is expected to resemble a shallow mixing layer developing between two parallel streams of unequal velocities. In stark contrast to Case 1, only patches of negative vertical vorticity are present inside the MI in the instantaneous flow fields in Case 2 (Fig. 3b). Examination of the evolution of these patches of negative vorticity shows that merging between neighboring patches occurs at times. This behavior of the VOVs inside the MI confirms the Kelvin–Helmholtz mode is dominant in Case 2 (see also sketch in Fig. 2a).

In Case 3 the confluence angle is close to zero, but the two close-to-parallel streams make an angle of close to 60° with the post-confluence channel. This induces strong curvature effects and results in the MI being pushed toward the west bank compared to Case 1. Though VR ≈ 1 close to the confluence apex, this is not the case away from it. Simulation results show that the ratio between the mean velocities on the two boundaries of the MI can reach values around 2 inside the CHZ. This means that the wake-like mode, if present, can be strong only close to the confluence apex. Simulation results show that the Kelvin–Helmholtz mode is the dominant within the downstream part of the MI, as confirmed by the instantaneous vertical vorticity field in Fig. 3c that shows the presence of patches of positive vorticity inside the MI. Curvature effects play an important role in the evolution of the VOVs. As the MI shifts toward the outer (right) bank, high velocity fluid situated close to the 'outer side' boundary of the curved MI damps the growth of the quasi two-dimensional MI eddies, which is one of the reason for the observed decay in the coherence of the VOVs past section A1. The more surprising result is the absence of patches of negative vorticity close to the confluence apex in Fig. 3c. This suggests that the wake-like mode is very weak despite VR and MR being close to one. The explanation is that no flow stagnation occurs close to the junction corner because of the streamlined shape of this corner. In such cases, the interaction of the separated shear layers on the two side of the confluence apex does not result in the shedding of patches of vorticity of opposite sign. So, Case 3 is representative of concordant confluences where the Kelvin–Helmholtz mode becomes stronger with increasing distance from the confluence apex along a curved MI. Case 3 is also a good example of a confluence with VR≈1 where the wake-like mode is very weak starting at the confluence apex. So, VR≈1 is a necessary but not a sufficient condition for the wake-like mode to be sufficiently strong to result in the formation of counter-rotating VOVs.

### 3.2 Streamwise-orientated vortices and effect of planform geometry

Figure 4a uses the Q criterion that identifies vortical structures in the flow [136] to visualize the main coherent eddies forming inside the CHZ in Case 1 for which VR ≈ 1. For such cases, one expects SOV cells to form on both sides of the MI. The SOV cells on the CS side are expected to be more coherent (e.g., higher circulation of their cores) due to the larger angle between the core of high velocity inside the CS tributary and the centerline of the MI. In most cases, the SOV cells in the mean flow are situated outside of the MI, though some of them can partially or fully penetrate inside the MI especially at large distances from the confluence apex. Consistent with the already discussed mechanism for the formation of SOV cells, the main SOV cells on the two sides of the MI (SVW1 and SVE1 in Fig. 4a) are counterrotating. Simulation results show the formation of secondary SOV

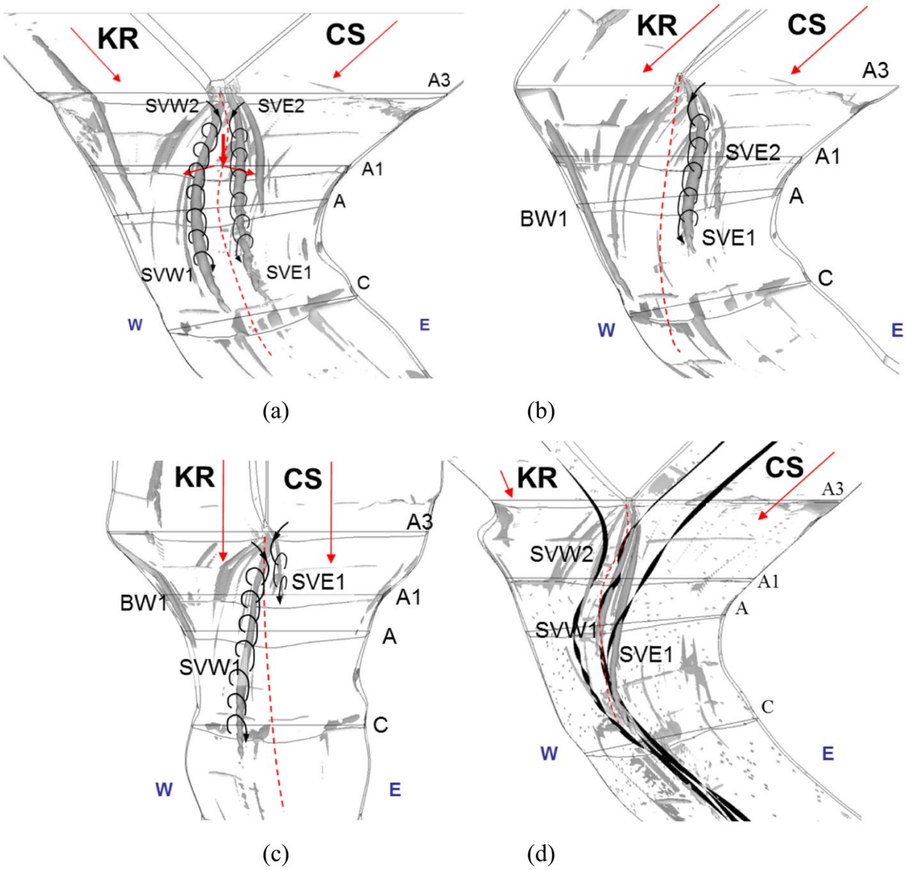


**Fig. 4** KRCS simulations with no density difference between incoming streams. Visualization of the main vortical structures in the mean flow using a Q iso-surface (Q = 10). **a** Case 1 (VR≈1, $\alpha_1 = 0°$; $\alpha_2 = 60°$); **b** Case 3 (VR≈1, $\alpha_1 = 60°$; $\alpha_2 = 60°$); **c** Case 4 (VR≈1, $\alpha_1 = 0°$; $\alpha_2 = 0°$); **d** Case 5 (VR≈5, $\alpha_1 = 0°$; $\alpha_2 = 60°$). The dashed red line shows the approximate position of the MI centreline. SVE1 and SVE2 are the SOV cells on the East (E) side of the confluence. SVW1 and SVW2 are the SOV cells on the West (W) side of the confluence. BW1 is a streamwise cell of helical flow forming at the West bank. The ribbons (thick black curves) in frame **d** show the large rotational capacity of the main SOV cells. Frames (**a**–**d**) are reproduced or adapted from Constantinescu et al. (31, 32)

cells on both sides of the MI. On each side of the MI, the circulation sign of the primary (SVW1 and SVE1) SOV cells and of the secondary SOV cells (SVW2 and SVE2) is the same. Secondary cells form when the near bed secondary flow is advected back toward the free surface over relatively large distances away from the MI. As a result, the secondary cells have the same sign of rotation as the primary cell on the same side of the MI. An analogy can also be made with secondary horseshoe vortices in junction flows. These vortices are also rotating in the same direction as the main horseshoe vortex and form in a region of strong adverse pressure gradients.

Case 1 suggests that SOV cells form on both sides of the MI at least for cases with VR ≈ 1. However, this is not always the case as illustrated in Fig. 4b for Case 3 where VR ≈ 1. The reason for the absence of SOV cells on the KR side of the MI is that the core of high momentum inside the KR tributary moves toward the west bank line. As a result, its exchange of momentum with the MI is negligible even if the centerline of the MI also moves toward the west bank line. By contrast, the core of high velocity inside the CS is oriented toward the MI. The strong adverse pressure gradients generated by the core hitting the MI result in the generation of a primary SOV cell (SVE1) and of a corotating secondary SOV cell (SVE2) of lower circulation on the CS side.

Given that the mechanism for the formation of SOV cells requires that at least one of the incoming streams is oriented at a large angle with respect to the MI, one would expect no SOV cells form at confluences with a small confluence angle. This is indeed the case for MIs between parallel streams forming in a constant-depth channel [25] but not necessarily the case for confluences with complex bathymetry as illustrated by Case 4 in Fig. 4c. Even though the two tributaries are parallel upstream of the confluence apex, the bank line on the west side is such that the KR stream increases its angle with respect to the MI and moves toward it as in enters the CHZ. By contrast, the CS stream is deflected slightly away from the MI toward the east bank line. Meanwhile, because of the strong curvature of the west bank downstream of the confluence apex, the flow accelerates on the KR side of the MI and stronger adverse pressure gradients are generated perpendicular to the MI on the KR side. This explains the formation of a fairly strong SOV cell (SVW1) on the KR side of the MI in Case 4 where the incoming streams and the post confluence channel are fairly parallel. A SOV cell (SVE1) forms on the CS side. However, this cell is very weak and plays a minor role in the redistribution of the streamwise momentum inside the CHZ.

In general, SOV cells are expected to be stronger on the high momentum side of the confluence (Constantinescu et al., 2010). Figure 4d visualizes the SOV cells forming at the KRCS confluence for a simulation conducted with VR ≈ 5. Though the angles between the cores of high velocities inside the two tributaries and the MI are comparable, the higher-momentum CS stream needs to lose more kinetic energy associated with the velocity component perpendicular to the MI as its core reorients itself parallel to the centerline of the post-confluence channel. Consequently, the adverse pressure gradients generated away from the MI are larger, which explains the larger coherence and larger penetration distance of the primary SOV cell (SVE1) on the CS side of the MI compared to the one (SVW1) forming on the lower-momentum side. For large MR and VR ratios, SOV cells may be very weak or even not form on the low momentum side of the MI.

Another fundamental feature of the dynamics of some of the most coherent SOV cells is the presence of bimodal aperiodic oscillations [31]. If such oscillations are present, the core of the SOV rather than simply oscillating around its mean position in the mean flow is subject large sweeping motions toward and away from the MI. As the core of the SOV cell moves toward the MI, its core becomes more circular and of smaller cross-sectional size. This state is referred as the interface mode (IM). Strong interactions between the SOV cell and the VOV vortices occur during the IM mode. As the SOV moves away from the MI and toward the corresponding bank line, its core enlarges, and its shape becomes closer to on ellipse. The cell enters the bank mode (BM). The presence of bimodal oscillations can be easily inferred from the velocity histograms at points situated inside the core of the SOV based on its position in the mean flow. Figure 5 shows such a histogram inside the core of SVE1 forming in Case 5. The histogram has a pronounced two-peak distribution, and the two peaks are associated with the two modes. By contrast, one-peak distributions are generally recorded inside the cores of the SOV cells that are not subject to bimodal oscillations and also inside the MI. The presence of two regions of high turbulent kinetic energy or pressure rms fluctuations inside the core of the SOV cell is another indication of the presence of aperiodic oscillations. An important observation is that SOV cells are generally not subject to bimodal oscillations along their entire length. Rather the bimodal oscillations are the strongest in the region where the core of high velocity from the tributary hits the MI and decay monotonically downstream of this region [31].

As a result of the aperiodic, low frequency transitions between the IM and BM modes the core of the SOV moves over a much larger part of the bed surface compared to cases when bimodal oscillations are absent. The capacity of an SOV cell subject to bimodal oscillations to entrain sediment is much larger than the one of an SOV of comparable coherence that does not undergo such oscillations. 30, 31 were the first to show that at angled confluences the largest bed shear stresses were recorded beneath the cores of the SOV cells rather than over the part of the post-confluence channel situated on the high-speed side of the MI or beneath the MI. Moreover, in simulations conducted with both VR≈1 and with VR> >1, the SOV cells with the largest capacity to entrain sediment were the ones subject to bimodal oscillations. These findings confirmed the validity of the conceptual model proposed by Paola (1997) that the SOV cells act as a pump of sediment by entraining sediment beneath their cores and then advecting it inside their cores before releasing it to the surrounding flow downstream of the CHZ. It indirectly confirmed their critical role in the formation of the scour hole at natural river confluences.

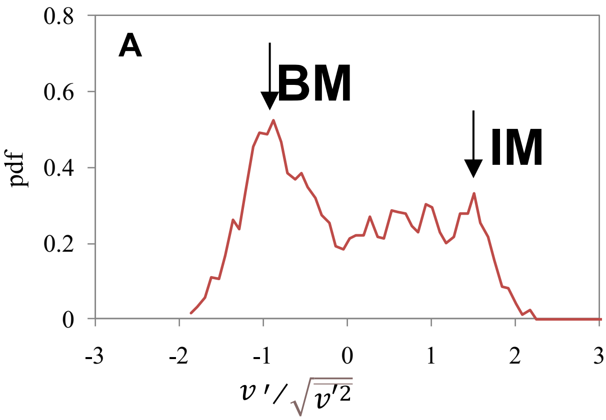


**Fig. 5** KRCS simulations with no density contrast. Probability-density functions of the vertical component of the instantaneous velocity fluctuations, $v'/\sqrt{\overline{v'^2}}$, for Case 5 (VR≈5, $\alpha_1=0°$; $\alpha_2=60°$) at a point situated close to the axis of the primary SOV cell on the East side (SVE1in Fig. 4d) in section A. The histogram of the instantaneous velocity shows that the large-scale oscillations of SVE1 are bimodal. The peaks associated with the bank mode (BM) and the interface mode (IM) are shown with arrows. Reproduced from Constantinescu et al. [32]

Besides their role in bed erosion, SOV cells play an important role in the redistribution of the streamwise momentum inside the CHZ and in mixing [29]. As opposed to the mixing associated with VOV vortices which is visible from the free surface, mixing driven by the SOV cells happens mostly beneath the free surface. The main mixing mechanism that is driven by VOVs is the engulfing of less-mixed fluid from one side of the MI by the VOV cells. Mixing by the SOV cells happens mostly because of the oscillations of the SOV cells that allow them to move temporarily inside the MI. As the coherence of the SOV cells is generally much larger than that of the VOVs, the SOV cells are very efficient at extracting mixed fluid from inside the MI.

Figure 6 visualizes the heat mixing between two streams of unequal temperature at the KRCS confluence via numerical simulations conducted with Ri = 0. The red and blue colors correspond to the mean temperatures of the unmixed fluid in the KR and CS streams, respectively. The capacity of the SOV cells to extract fluid from the MI increases significantly for the SOV cells that are subject to bimodal oscillations. For example, both primary SOV cells undergo bimodal oscillations in Case 1 and these oscillations peak near section A shown in Fig. 6a. The main effect on mixing associated with SVE1 and SVW1 is that their cores extract mixed fluid from the MI in the near-bed region and then advect it away from the MI. This is possible given that they rotate in opposite directions and that their rotation is such that they move fluid away from the MI near the bed. In terms of the mean temperature field, a direct consequence of the presence of the SOV cells is the increase of

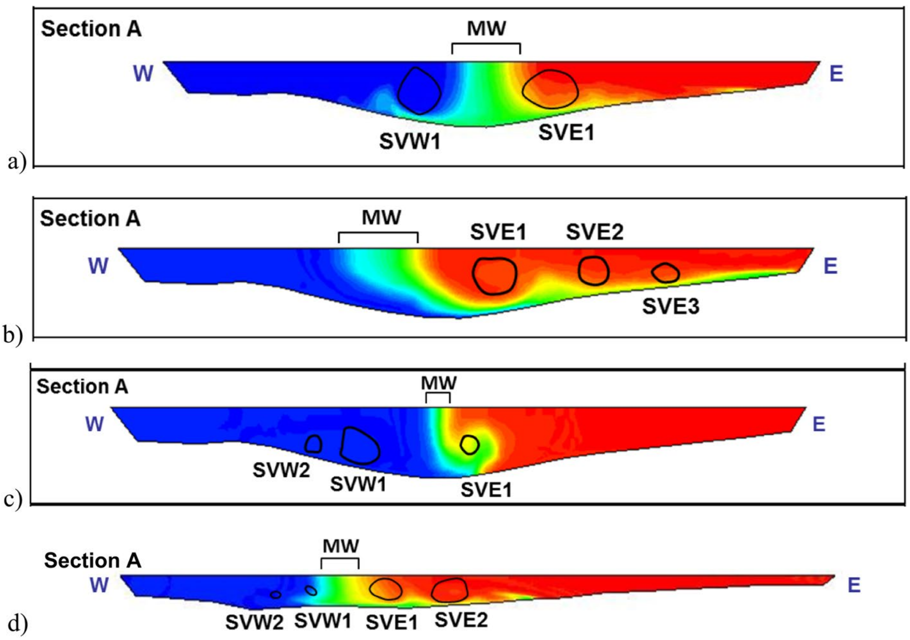


**Fig. 6** KRCS simulations with no density contrast. Visualization of thermal mixing in the mean flow at section A. **a** Case 1 (VR≈1, $\alpha_1 = 0°$; $\alpha_2 = 60°$); **b** Case 3 (VR≈1, $\alpha_1 = 60°$; $\alpha_2 = 60°$); **c** Case 4 (VR≈1, $\alpha_1 = 0°$; $\alpha_2 = 0°$); **d** Case 5 (VR≈5, $\alpha_1 = 0°$; $\alpha_2 = 60°$). The nondimensional time-averaged temperatures of the incoming flow in streams KR and CS are TNM = 0 (blue color) and TNM = 1 (red color), respectively. The black circles visualize the cores of the main SOV cells in the mean flow. MW denotes the width of the MI at the free surface. Reproduced from Constantinescu et al. [33]

the width of the thermal MI as the bed is approached (Figs. 4a and 6a). This effect is even stronger in Case 3 (VR≈1) where a strongly coherent primary SOV cell forms very close to the MI together with two co-rotating secondary SOV cells (Figs. 4b and 6b). The near-bed mixed fluid extracted by SVE1 is then further advected toward the banks by the cores of the secondary SOV cells. The result is the formation of a long near-bed intrusion of mixed fluid. At section A this intrusion penetrates until the east bank. A similar effect of the SOV cells on the temperature distribution in the cross sections is also observed in Case 5 (VR > > 1) where the level of coherence of the SOV cells on the east side of the MI is much larger compared to that of the cells forming on the west side (Figs. 4d and 6d). The difference in the coherence level of the SOV cells explain why on the west side the near-bed intrusion is fairly small, while on the east side the width of the intrusion is 4–5 times larger than the average width of the MI away from the bed. Even in Case 4 where the incoming streams are close to parallel to the post-confluence channel (Fig. 4c), the primary SOV cell strongly disturbs the thermal MI (Fig. 6c). However, rather than advecting the extracted mixed fluid toward the banks, this fluid is mostly entrained inside its core. These examples clearly show that strongly-coherent SOV cells can significantly amplify the amount of mixed fluid within and downstream of the CHZ and increase the vertical non-uniformity of the temperature field in these regions even in the absence of density stratification.

## 4 Stratification effects at concordant bed confluences due to density contrast between the incoming streams

If the flows in the two tributaries have unequal densities due to differences in temperature, salinity and/or suspended sediment concentrations, a vertical density interface is present downstream of the confluence apex. This density interface is unstable because of differences in the hydrostatic pressure on its two sides. Assuming density contrast is sufficiently large to induce buoyancy forces that are of comparable magnitude to the inertial forces, the density interface will start deforming with increasing distance from the confluence apex. A near-bed intrusion of heavier fluid starts moving toward the opposing bank while the opposite happens near the free surface where an intrusion of lighter fluid forms. This is equivalent to the formation of a spatially-evolving lock-exchange-like flow [28]. Given that the MI 'moves' in opposite directions near the bed and near the free surface, the MI is strongly tilted at confluences where density contrast effects are significant. The flow evolves toward a stable configuration where the lighter fluid moves on top of the denser fluid. This generally happens when the two intrusions reach the channel banks.

Recent research (e.g., see Cheng and Constantinescu, 2022b; [86],Ramon et al., 2013, 2016; [66, 89, 97],Jiang et al., 2022) have shown that near-bed intrusions of heavier fluid are generally observed at concordant bed confluences where the Richardson number, Ri, is larger than 0.01. This value corresponds to a minimum densimetric Froude number, $Fr_d = 1/Ri^{0.5}$ of 10. Recently, Horna-Munoz et al. [66] showed that once the Richardson number starts approaching one, the flow originating in the tributary containing lighter fluid moves over the heavier fluid originating in the other tributary such that the free-surface regions containing heavier and lighter fluid switch sides in the downstream part of the post-confluence channel. Such cases are referred to as strong stratification cases. These effects are discussed next based on simulations and field experiments conducted at a small-size (average flow depths in the main channel less than couple of meters) and small-scale (width over depth ratio less than 20) confluence (KRCS confluence in the USA), at a medium-size (average flow depths of the order of tens of meters) and large scale (width over depth ratio larger than 50) confluence (confluence between the Yangtze River and Poyang Lake tributary in China) and at the confluence between the Negro River and the Solimoes River in the Amazon, which is one of the largest confluences in the world.

### 4.1 Generation of a spatially-developing, lock-exchange-like flow in transverse *planes* for moderate stratification (0.01 < Ri < < 1)

Horna-Munoz et al. [66] reported simulations conducted at the KRCS confluence with and without density difference. In particular, they performed a series of three simulations (Case 1 to Case 3 in Fig. 7) with VR = 1.33 and MR = 2.1. In Case 1 the CS tributary contains the lighter, higher temperature fluid while in Case 3 the CS tributary contains the denser fluid. In both cases, Ri = 0.04 and $Fr_d = 4.9$. A third simulation (Case 2) was performed with the same flow and temperature conditions as in Case 1 but with Ri = 0 (e.g., the coupling between the temperature/density equation and the momentum equations was removed in the numerical solver) such that temperature-induced stratification effects are ignored. The flow and temperature conditions in Case 1 correspond to those in a field experiment conducted by Lewis and Rhoads [86].

Figure 7 shows the distributions of the nondimensional temperature/scalar concentration $C = (T_{CS}-T)/(T_{CS}-T_{KR})$, where T is the dimensional temperature field, $T_{CS}$ is the temperature of the fluid in the CS stream and $T_{KR}$ is the temperature of the fluid in the KR stream. Comparison of the distributions of C near the free surface (Fig. 7a) and in a near-bed surface parallel to the bed (Fig. 7b) shows very large differences in the position and size of the regions containing unmixed and mixed fluid. In particular, the MI near the free

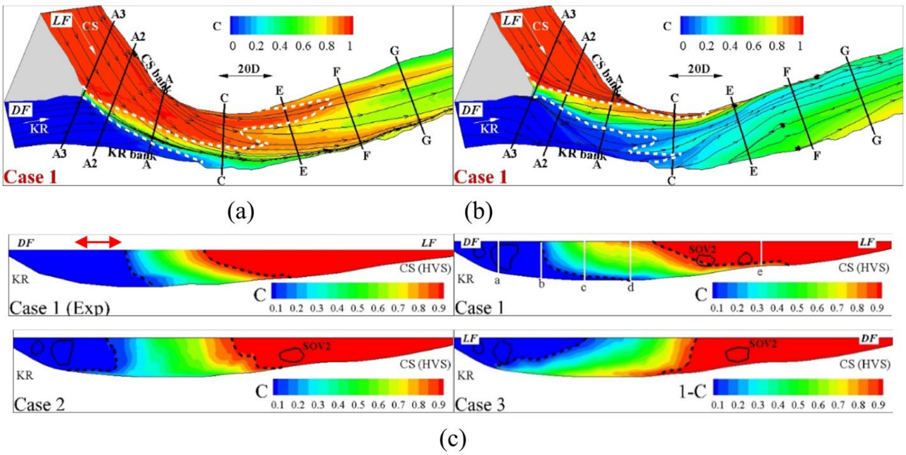


**Fig. 7** KRCS simulations with and without density contrast. Mean nondimensional temperature/concentration, C, in the Ri = 0 (Case 2) and Ri = 0.04, $Fr_d = 4.9$ (Case 1 and Case 3) simulations conducted with VR = 1.33. **a** C at the free surface in Case 1; **b** C near the bed in Case 1; **c** C in cross section A. Also shown in frames **a** and **b** are 2-D mean streamline patterns. The two dashed lines correspond to C = 0.1 and C = 0.9. DF and LF denote the stream containing denser and, respectively, less dense fluid. Also shown in frame c) are the main SOV cells and the main cross-stream cell of secondary motion forming close to the KR bank (Cases 1 to 3). HVS denotes the high velocity stream. Case 1 (exp) shows field measurements of the mean temperature for Case 1. Reproduced from Horna-Munoz et al. [66]

surface moves toward the right (KR) bank, which is reached around section C. By contrast, the MI near the bed approaches the left (CS) bank near the bed. The width of the MI is significantly larger near the bed compared to near free surface region.

The movement in opposite directions of the MI near the bed and the free surface is fully consistent with the development of a lock-exchange-like flow in Case 1 as the denser fluid in the KR stream start intruding near the bed into the LF side of the post-confluence channel. As this happens, the lighter fluid from the CS stream situated close to the free surface is pushed toward the KR bank with increasing distance from the confluence apex. Figure 7c visualizes the near bed and free-surface intrusions in section A which result in a strong tilt of the region containing mixed fluid in Case 1. The predicted temperature distribution is in good agreement with the one measured in a field experiment. Comparison of the temperature distributions in section A between Case 1 and Case 2 proves that the tilt of the MI is due to stratification effects and not to the deformed bathymetry and formation of SOV cells. Indeed, if the effect of the temperature on the velocity field is ignored (Ri = 0), the temperature distribution inside the CHZ becomes fairly uniform over the flow depth except near the edges of the MI where the SOV cells induce more mixing near the bed (see Case 2 in Fig. 7c). However, there is no tilt of the MI and no near bed intrusion of unmixed KR fluid beneath the MI, as seen in Case 1. The predicted distributions of C in Case 2 are in poor agreement with the measured ones at the same section. This shows the critical role played by stratification in this case. The temperature distribution in section A in Case 3 also shows a strong tilt of the MI but the tilt is in the opposite direction. This is because the inversion of the streams containing denser and lighter fluid means that the lock exchange flow in Case 3 develops in opposite directions near the free surface and near the bed with respect to Case 1. Finally, the region of mixed fluid situated downstream of section C in Fig. 7b is mostly due to the lighter, free-surface fluid reaching the KR bank and then plunging down and mixing with the heavier fluid situated below it. So even for cases with moderate density effects, temperature distribution away from the apex is mainly determined by stratification effects. The SOV cells, though still present, play a secondary role in mixing compared to mixing driven by the spatially-developing lock-exchange-like flow. VOVs still form in Case 1 and Case 3, but they are severely stretched away from the confluence apex and rapidly lose their coherence.

One important research question is if the development of a lock-exchange-like flow is a general characteristic of flow hydrodynamics at confluences with sufficiently strong density contrast between the incoming streams and can be observed at confluences whose scale and size are much larger than those of KRCS where the mean flow depth is less than 1 m and the mean free-surface width to mean depth aspect ratio less than 20. The development of a lock-exchange-like flow at larger-size confluences was investigated by Jiang et al. (2022) for the confluence between the Yangtze River (YR) and the Poyang Lake (PL) in China (defined as YRPL), which is classified as a large-scale confluence given that the ratio between the mean free-surface width and mean depth, D, of the post-confluence channel is about 60. The YRPL confluence is an asymmetric, concordant confluence for which the mean angles between the downstream channel and the two tributaries are $\alpha_1 \approx 0°$ and $\alpha_2 \approx 58°$. The YR tributary contains warmer water during the winter and colder water during the summer compared to the PL tributary. A large scour hole is present on the PL side of the post-confluence channel starting about 60D from the confluence apex (Fig. 8a). Its maximum depth is about 2.8D. Flow conditions in the simulations (VR = 0.78, Mr = 0.36, where the YR tributary was the faster one) were determined based on the field survey. A first simulation (Case 1) was conducted with a difference of 2.5 °C between the YR and PL tributaries but neglecting stratification effects (Ri = 0). Stratification effects were included

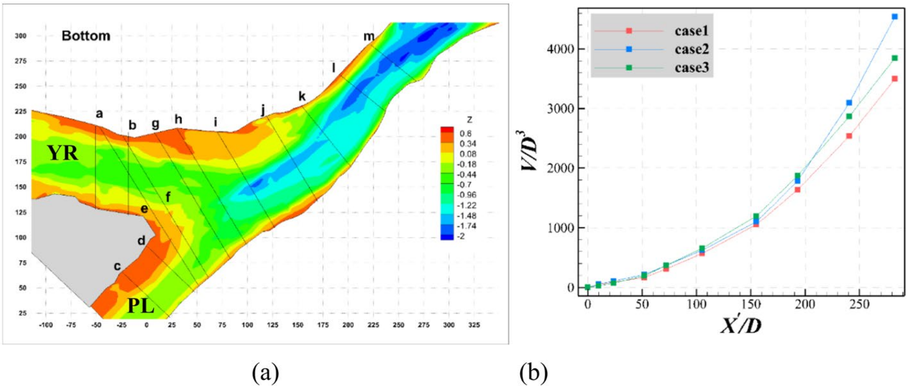


**Fig. 8** YRPL confluence of Yangtze River (YR) and Poyang Lake channel (PL). **a** Bathymetry. The 2–D contours show the vertical elevation, z/D, where z is the vertical distance and z/D = 0.68 corresponds to the free surface; **b** Nondimensional volume of mixed fluid, V/D.$^{3}$, as a function of the streamwise distance from the confluence apex, X'/D. Reproduced from Jiang et al. [70]

in Case 2 for which Ri = 0.037 and $Fr_d = 5.2$. Case 3 simulation was conducted with same values of Ri and $Fr_d$ as for Case 2, but with the warmer water present in the PL tributary.

One striking feature of the nondimensional temperature distribution in section C (Fig. 8a) for Case 1 is the strong tilt of the MI, with some of the mixed fluid from inside the MI intruding into the YR side of the post-confluence channel. This happens in the absence of stratification effects and even in the absence of SOV cells. The tilt is driven by topographic steering and by the formation of a strong cell of secondary flow on the YR side that basically touches the boundary of the MI (Jiang et al., 2022). So, the presence of a tilted interface in field or lab measurements does not automatically signals significant stratification effects and the generation of a lock-exchange flow. One should also point out that the bottom intrusion does not increase monotonically in the streamwise direction at sections situated downstream of section C for Case 1, as it will be expected to happen for a spatially developing lock exchange flow.

Once stratification effects are incorporated into the numerical model, the mean temperature distribution changes significantly. In Case 2, where the PL tributary contains the denser fluid, the tilting of the MI is expected to occur in the same direction as for Case 1. So, stratification should enhance the tilting of the MI compared to non-stratified flow conditions. This is exactly what is observed in Fig. 9b where the near-bed intrusion of heavier fluid on the PL side and free-surface intrusion of lighter fluid on the YR side are much stronger compared to Case 1. The same is true for the lateral penetration distance of the intrusion containing mixed fluid on the YR side that more than doubles its length. On the other hand, if the streams containing heavier and lighter fluids are reversed, the stratification driven intrusions of heavier and lighter fluid should develop in opposite directions compared to Case 2 and thus should counter-act the tilting observed for non-stratified flow conditions (Case 1). This is indeed what happens in Fig. 9c where the tilt of the MI is in the opposite direction compared to Case 2. The tilt is not as high as for Case 2, but this is simply because the intrusion of heavier fluid driven by density contrast develops into a flow field that forces the MI to be tilted in the opposite direction. However, in both Case 2 and Case 3 stratification effects are significant and consistent with those observed at the KRCS confluence.

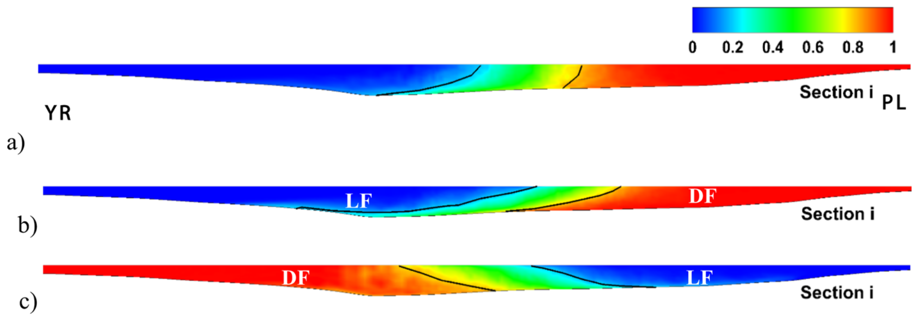


**Fig. 9** PLYR simulations with and without density contrast. Non-dimensional density/temperature, C, at cross section i in the mean flow. The solid black lines (C = 0.2 and C = 0.8) visualize the edges of the mixing interface region. **a** Case 1, Ri = 0, VR = 0.78; **b** Case 2, Ri = 0.037, VR = 0.78, PL contains denser fluid (DF); **c** Case 3, Ri = 0.037, VR = 0.78, PL contains lighter fluid (LF). Reproduced from Jiang et al. [70]

Another important research question is whether density effects enhance rather than inhibit rates of mixing at confluences. The way flow stratification affects large-scale coherent structures and mixing is much more complex at river confluences, where the flow is shallow and, at the same time, highly three dimensional, compared to deep mixing layers forming between streams of unequal densities. Although density difference may damp the rate of growth and coherence of VOVs inside the MI, other mixing mechanisms are amplified and new mixing mechanisms, such as an increase in the length of the MI and the formation of streamwise vortices at the interface between the lighter and heavier fluids can develop. The intrusions of heavier and lighter fluid may also generate additional cells as they approach the banks (Cheng and Constantinescu, 2022b) while strong mixing generally develops as these intrusions directly interact with the banks and flow is pushed upwards or downwards.

One simple way to quantify mixing is to calculate the variation of the volume of mixed fluid, V, with the streamwise distance measured from the confluence apex, X'. Figure 8b compares the variations of V for the simulations conducted for the YRPL confluence with and without density contrast. The mixed fluid is defined as fluid with $0.2 < C < 0.8$. The total amounts of mixed fluid are greater for cases with density effects (Ri = 0.037) than for cases where stratification effects are neglected (Ri = 0). The same is true for the simulations conducted with Ri = 0 and Ri = 0.04 at the KRCS confluence. This is an important finding that may be contradicted based on simple observation of mixing at confluences evaluated based on the mixing observable at the free surface. If stratification effects are significant, most of the mixing induced by stratification driven mechanisms happen beneath the free surface. In fact, in some of the simulations conducted with $Ri > 0$, the width of the MI at the free surface was relatively small, which would indicate weak mixing between the converging streams. However, mixing away the free surface can be very strong and compensate for the relatively low rates of mixing present near the free surface. So, for such cases, information on the 3-D distribution of the variable used to assess mixing (e.g., temperature, turbidity) is needed to make accurate predictions.

Four field surveys based on ADCP and conductivity measurements were conducted under different flow conditions in 2020–2021 near the confluence between the Yangtze River and the Poyang Lake, which are the largest river and freshwater lake in China, respectively (Fig. 10). It was found that mixing dynamics at the confluence was controlled

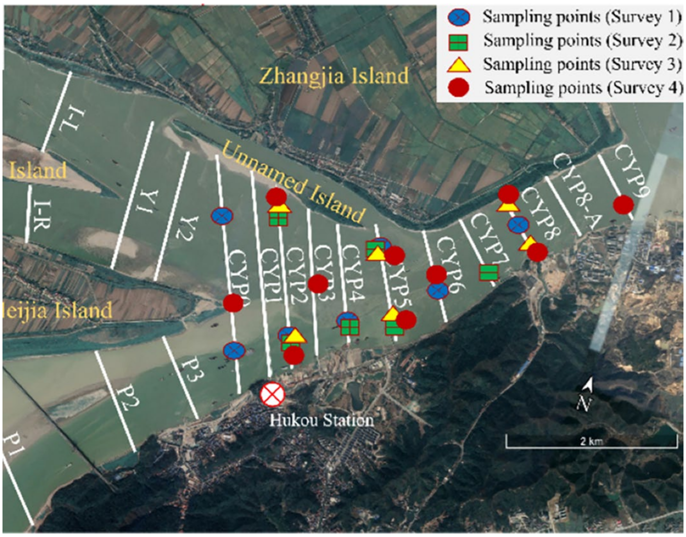


**Fig. 10** Map of measurements locations at the confluence between the Yangtze River and the Poyang Lake during four surveys in 2020–2021: The white lines indicate cross sections for ADCP measurement, while the symbols indicate water chemistry sampling points. Reproduced from Xu et al. [162]

by the complex interaction between the seasonal changes of the momentum flux ratio, which affect the secondary flows (Fig. 11), and the lock-exchange flow associated with density contrast between the two tributaries (Fig. 12).

The mixing processes were studied using the vertical profiles of water conductivity and backscatter intensity at key locations of the confluence. The streamwise development of mixing was estimated using a normalized mixing metric based on calculating the standard deviation of the conductivity at each cross-section inside the CHZ as well as at an upstream composite cross-section consisting of conductivity for the two incoming flows [86]. Slow mixing (e.g., mixing distance larger than 5 km) was observed during high-flow conditions in which dual counter-rotating secondary cells formed, with the downwelling flow acting as a barrier in the post-confluence channel (Fig. 11a). By contrast, more rapid mixing (mixing distance close to 2.5 km) was observed during low-flow conditions when only an anticlockwise single channel-scale secondary flow pushing near the bed Yangtze River waters into Poyang Lake waters was identified (Fig. 11b). The lock-exchange flow can work to strengthen or to weaken such secondary flow structures (Fig. 12). In low-flow conditions, when the Yangtze River waters had higher temperature that is, lower density than that of the Poyang Lake, buoyant forces reinforce secondary currents enhancing mixing (Fig. 12b). When the Yangtze River waters were denser, the density-driven exchange acted against the secondary flow, which resulted in slow mixing (Fig. 12a).

Two field surveys were carried out in 2014–2015 at the confluence between the Negro and Solimões rivers in the Amazon Basin. The surveys were carried in both low (October 2014, FS – CNS1 campaign) and relatively high flow conditions (April/May 2015, FS – CNS2 campaign) (Trevethan et al., 2015a; 2016; [56, 57, 67]). During these campaigns, acoustic Doppler velocity profiling (ADCP) and high-resolution acoustic and seismic methods, such as echo-sounding and sub-bottom profiling, as well as a multi-parametric probe, were used.

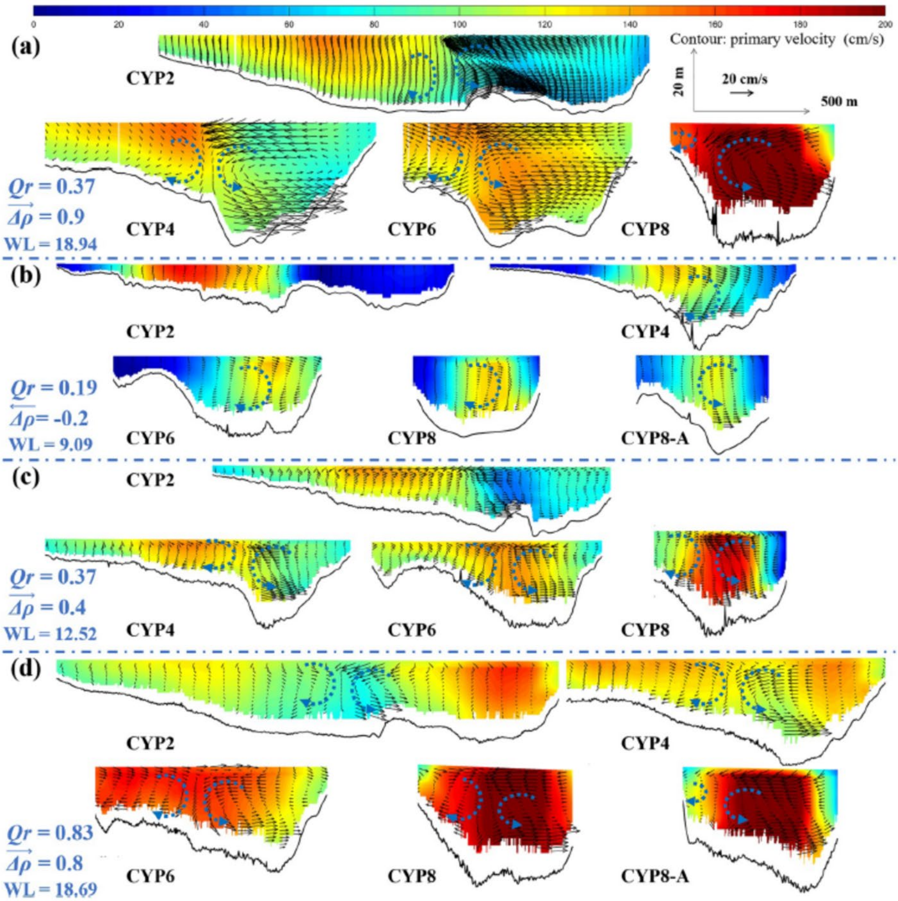


**Fig. 11** Secondary flows in representative cross sections for **a** Survey 1; **b** Survey 2; **c** Survey 3; **d** Survey 4, looking downstream (vectors: secondary velocity; contour: primary velocity; WL: water level with units of m). Reproduced from Xu et al. [162]

In the Negro River tributary, at the transects situated immediately upstream of the confluence, the depth – averaged velocity was relatively low (≈ 0.30 m/s) and uniform over the channel width. In the Solimões River, the depth-averaged velocity distribution varied over the channel width. The velocities were close to 2 m/s in the FS-CNS1 survey and 2.5 m/s in the FS – CNS2 survey in the main channel, near the right bank. The velocities decreased towards the left bank to approximately 1 m/s in both surveys (Fig. 13).

The distribution of the depth-averaged velocity and surface temperature at the CNS0 and CNS8 transects, which were located approximately 220 and 200 m downstream of the junction, revealed a large difference in depth-averaged velocity magnitude between the Negro side and the Solimões side, with a sharp drop across the shear layer/mixing interface (Fig. 14). A sharp drop in temperature was also observed (Fig. 14a). For low flow conditions, the width of the region characterized by high velocity gradients was of the order of hundreds of meters. For relatively high flow conditions, the width was narrower, i.e. of the order of tens of meters, or even less.

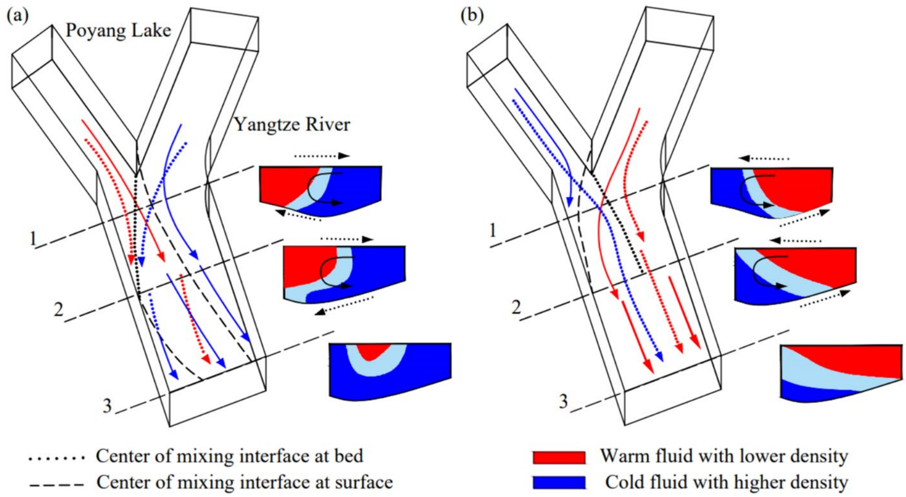


**Fig. 12** Conceptual model showing patterns of lateral mixing between two flows with different densities at the confluence of Yangtze River and Poyang Lake. **a** the Yangtze River contains denser fluid than Poyang Lake, and **b** Poyang Lake contains denser fluid than the Yangtze River. Red arrows correspond to flow from the Yangtze River and blue arrows correspond to flow into the Poyang Lake. Solid arrows represent flow near the surface and dashed arrows represent flow near the bed. Curved arrows in a cross-section denote strong, curvature-induced cells of helical flow, while the dashed arrows show the development of the near-bed and free-surface intrusions associated with the lock-exchange like flow. Dark blue corresponds to unmixed cold fluid of higher density. Red corresponds to unmixed warm fluid of lower density. Light blue corresponds to mixed fluid inside the mixing interface. Reproduced from Xu et al. [162]

In the CNS0 transect, the difference between the depth-averaged velocity magnitude in the Negro and Solimões rivers, i.e. $\Delta V_{depth\text{-}avg}$, was about 0.90 m/s in the FS-CNS1 survey and more than 1.0 m/s the FS – CNS2 survey. Between transects A0 situated near the confluence apex and A14, the median depth-averaged velocities of the Solimões portion decreased, while those of the Negro portion increased, so $\Delta V_{depth\text{-}avg}$ decreased (Fig. 15a). This indicates strong transfer of momentum from the Solimões to the Negro side of the Amazon Channel due to velocity shear. At transect A16, $\Delta V_{depth\text{-}avg}$ ≈0.05 m/s in the FS – CNS1 survey. By contrast, a velocity difference of about 0.6 m/s was still observed in the FS-CNS2 survey (Fig. 15a). At the most downstream transect A8, the difference was about 0.19 m/s (Fig. 15a). Overall, $\Delta V_{depth\text{-}avg}$ was larger for low-flow conditions, both immediately upstream and downstream of the junction apex, while the transfer of momentum from the Solimões to the Negro side of the Amazon Channel was comparatively weaker in high-flow conditions than in low-flow conditions. The same trend was observed for the difference in the backscatter signal, $\Delta BS_{depth\text{-}avg}$ (Fig. 15b).

Figure 16 presents the distribution of the backscatter intensity at cross sections CNS0, CNS1 and A13 on 31/10/2014 during the FS−CNS1 survey. Red color indicates the sediment rich waters of the Solimões River and blue color indicates pure Negro waters. A sharp drop in backscatter intensity between the tributaries was observed across the MI at transect CNS0. Further downstream, for both flow conditions, the MI was subjected to a complex development because of the plume (e.g., near-bed intrusion) of sediment-laden flow that moved close to the bed from the Solimões side into the Negro portion. The propagation of this plume, that is consist-

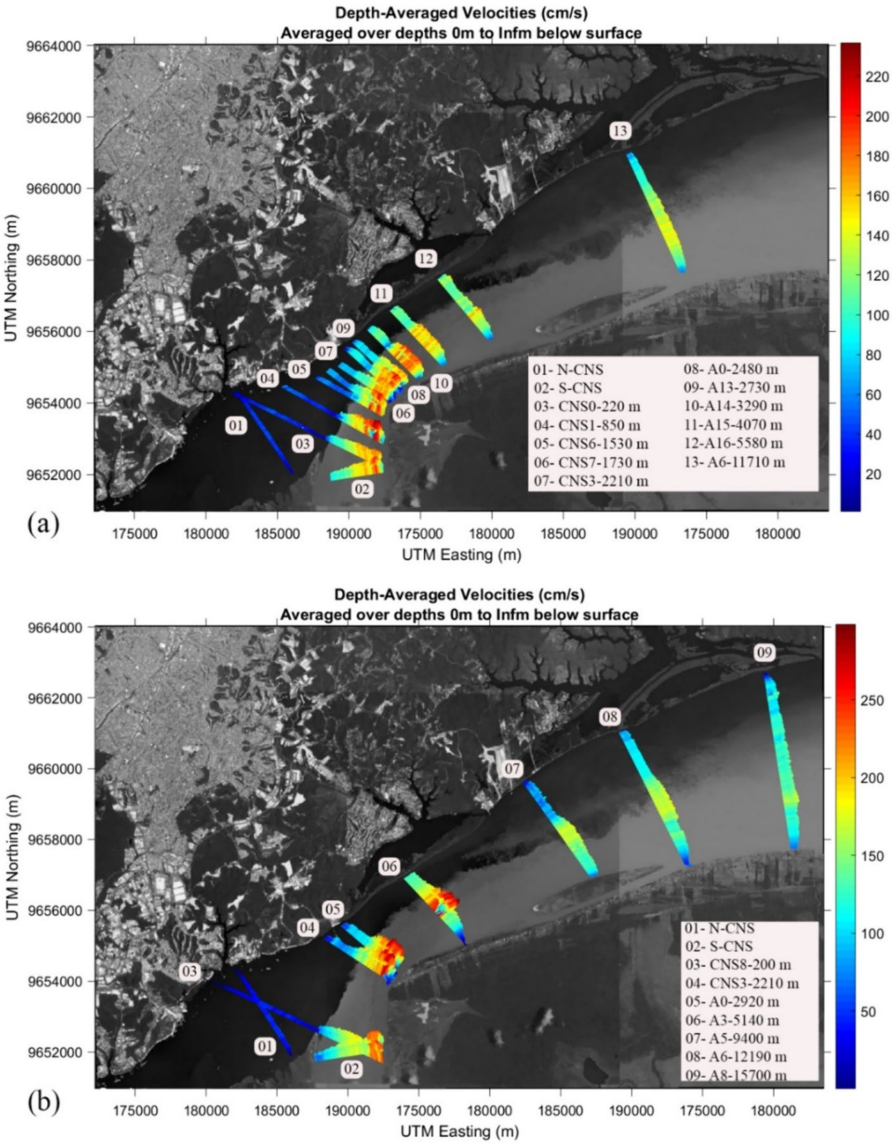


**Fig. 13** Depth-averaged velocities of ADCP transects collected at the confluence of the Negro and Solimões Rivers on 30–31/10/2014 (**a**) and on 29–30/04/2015 (**b**) during FS – CNS1 and FS – CNS2 surveys, respectively

ent with the development of a lock-exchange flow, could be clearly observed by comparing the backscatter intensity at transects located downstream of transect CNS0. Third, the sediment-laden flow interacted with water of the Negro side (Fig. 16b–c), as well as with the confluence bathymetry (Fig. 16b), resulting in upwelling of sediment-rich waters that, at some locations, reached the water surface (Fig. 16c). The distributions of the backscatter intensity demonstrated that the MI at the Negro/

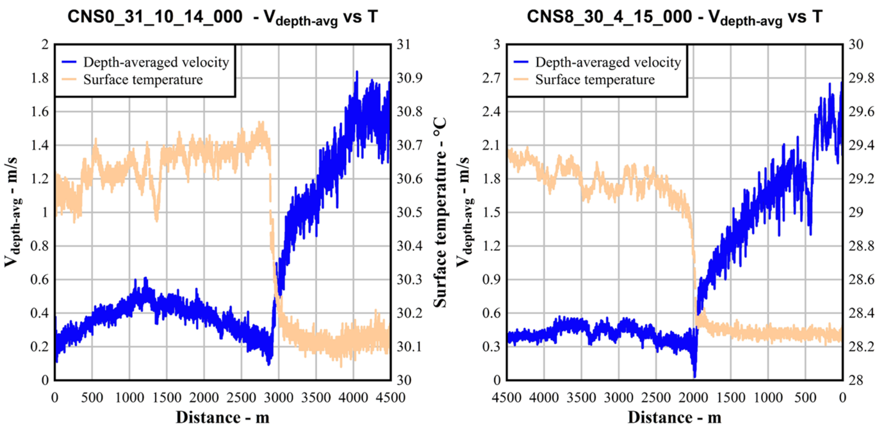


**Fig. 14** Depth-averaged velocity magnitude and temperature on 31/10/2014 (**a**) and on 30/04/2015 (**b**) at the entrance of the confluence hydrodynamic zone. Reproduced from Gualtieri et al. [57]

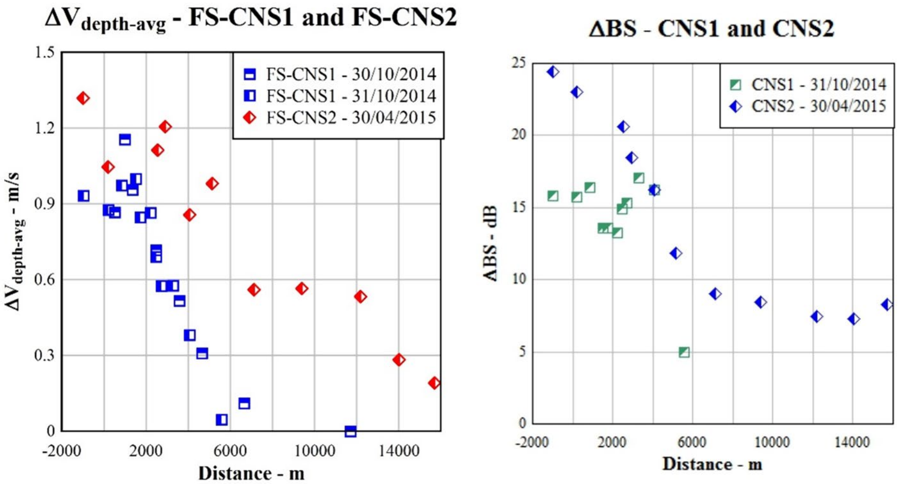


**Fig. 15** Difference in depth-averaged velocity magnitude (**a**) and in backscatter intensity (**b**) between the Negro and Solimões Rivers sides of the post-confluence channel during FS-CNS1 and FS-CNS2. Reproduced from Gualtieri et al. [56]

Solimões confluence is not vertical but is tilted due to the interactions among the different processes controlling mixing. This is consistent with previous field observations at the same confluence [82] and at other confluences with strong density differences [81],Ramón et al., 2013; [65] as well as with the observed development of a lock-exchange-like flow at confluences with sufficiently strong density contrast in the aforementioned numerical studies.

Figure 17 shows the boundary of the MI at the water surface and at the bed along the CHZ for both flow conditions. Both at the water surface and at the bed, the MI for relatively high flow conditions was closer to the Negro bank compared to low flow

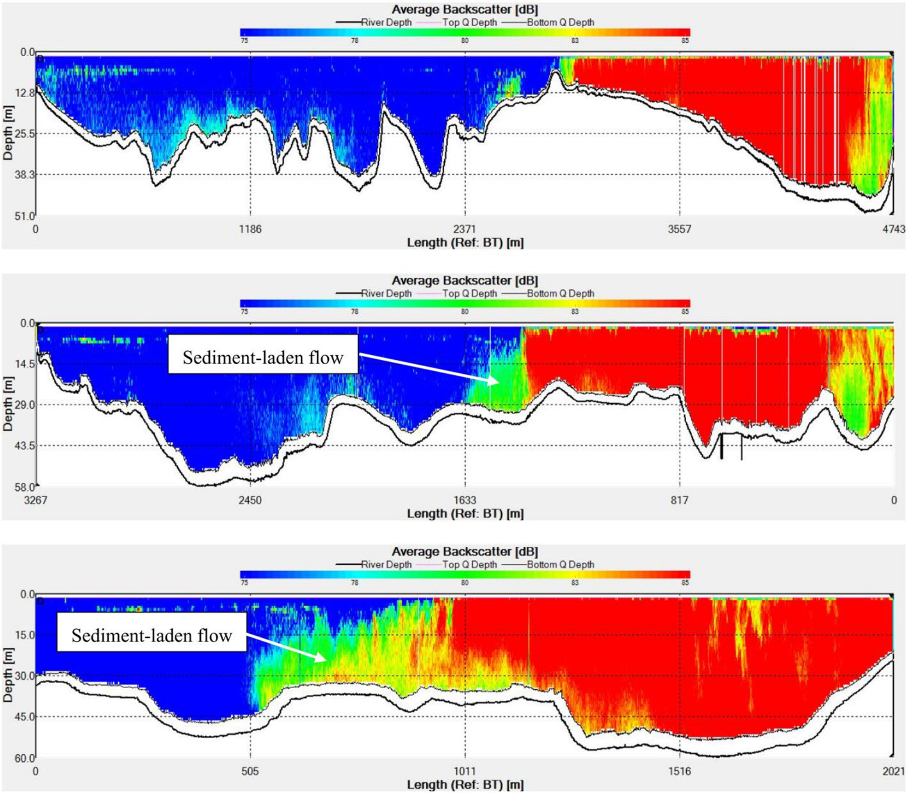


**Fig. 16** Distribution of the backscatter intensity for transects CNS0 (**a**), CNS1 (**b**) and A13 (**c**) on 31/10/2014 during the FS – CNS1 survey. The Negro and Solimões rivers are on the left and on the right, respectively. Reproduced from Gualtieri et al. [57]

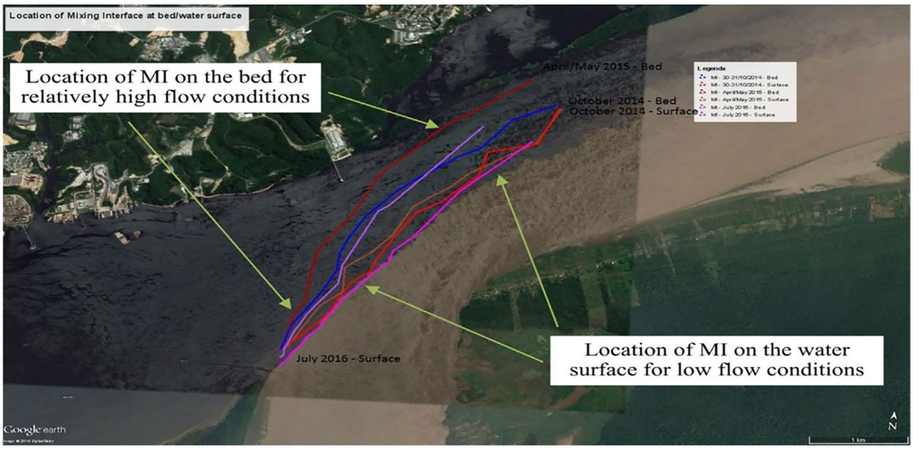


**Fig. 17** Map of the central part of the CHZ showing the location of the boundary between the MI and the region containing no sediments at the water surface and at the bed during the FS – CNS1 and FS – CNS2 surveys. Reproduced from Gualtieri et al. [57]

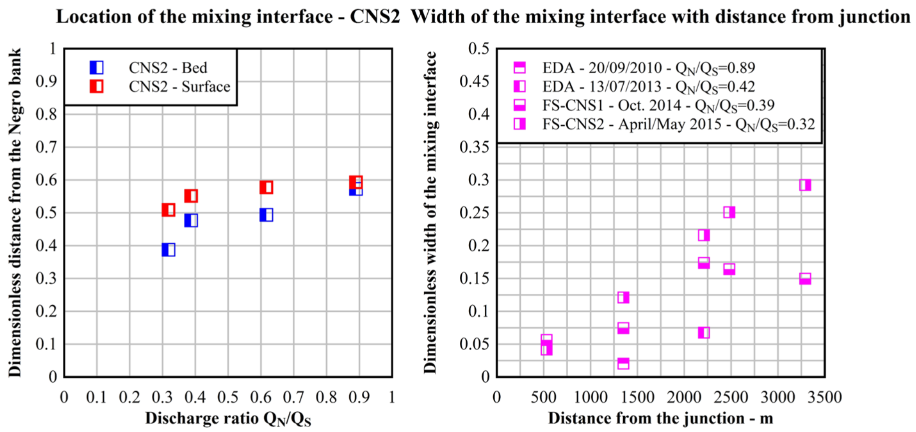


**Fig. 18** Dimensionless distance from the Negro bank vs. discharge ratio $Q_R$ at transect CNS2 (**a**) and the dimensionless MI width vs. distance from the confluence apex (**b**) during the EDA 2010, EDA 2013, FS – CNS1 and FS – CNS2 surveys. Reproduced from Gualtieri et al. [57]

conditions. The location of the boundaries and the width of the MI at the water surface and close to the bed are plotted with the discharge ratios $Q_R$=$Q_N/Q_S$ in Fig. 18a. The dimensionless distance from the Negro bank to the centerline of the MI at the water surface and at the bed was computed at CNS2, which was located 1.35 km downstream of the junction apex (Fig. 13). The distance was divided by the channel width at CNS2 when plotted in Fig. 18a. For all flow conditions, the MI at the bed was closer to the Negro bank than at the water surface. Finally, the distance from the Negro bank decreased with decreasing $Q_R$. The MI width, defined as the distance between the location of the MI boundary close to bed and at the water surface, was the largest for the lowest $Q_R$. Figure 18b also includes some data from two other surveys conducted in September 2010 (EDA 2010 $Q_R$=0.89) and July 2013 (EDA 2013 $Q_R$=0.42). During EDA 2010 ($Q_R$=0.89), the MI width in CNS2 was approximately 60 m. The MI width increased with the distance from the junction apex and was closely related to the discharge ratio $Q_R$. This means that the distance between the location of the MI boundary at the bed and at the water surface was larger as the difference between the discharges of the Solimões and Negro tributaries increased. The same trend was observed for the momentum ratio. Overall, this field data demonstrated that MI dynamics is closely related to the flow and velocity conditions in the tributaries confirming findings from recent field studies (e.g., see [81, 86, 97]).

### 4.2 Flow structure and mixing processes at confluences with strong density stratification

If the density difference between the incoming streams and the confluence angles are sufficiently large (e.g. the Richardson number approaches unity), the flow from the tributary containing the denser fluid plunges beneath the flow originating in the tributary containing lighter fluid that continues to advance near the free surface with little change in its initial direction. Both currents try to maintain their momentum alligned with the axes of the two tributary channels. As a result, these currents of denser and lighter fluid reach the opposite bank in the downstream part of the CHZ. The treshold value needed for the regions containing heavier and lighter fluid to switch sides inside the post-confluence channel depends on many factors besides the Richardson number but such inversions are generally observed for $Ri > 0.25$ ($Fr_d < 2$).

Figure 19 illustrates this phenomenon for the KRCS confluence based on the Case 6 simulation in the study of Horna-Munoz et al. [66]. The geometry and flow conditions were identical to those in Case 1 (Fig. 7a, b) except that the Richardson number was increased to 0.39, corresponding to $Fr_d = 1.6$. Near the free surface (Fig. 19a), the unmixed lighter fluid from the KR tributary reaches the opposite (CS) bank slightly upstream of section E. By contrast, no unmixed heavier fluid originating in the CS tributary is seen near the free surface downstream of section C at the CS bank. This is because this unmixed fluid plunges down (see PL line denoting the left boundary of the MI region at the free surface in Fig. 19a) and then advanced beneath the free surface toward the KR bank that is reached slightly downstream of section A (Fig. 19b). As this happens, heavier fluid is pushed back toward the free surface in the very shallow region bordering the KR bank and lots of mixing takes place. This is the main mechanism for the formation of the free-surface (MF) region containing mixed fluid on the KR side of the post-confluence channel visible in Fig. 19a. Consistent with the development of the lock-exchange flow, the MI extends between the confluence apex and section C at the CS bank near the free surface and in between the confluence apex and section A at the KR bank near the bed. Downstream of section E, the post-confluence channel contains near the free surface light unmixed fluid on its CS side and heavier, mixed fluid on its KR side. Such a phenomenon is impossible to happen in the absence of strong density contrast between two incoming flows. Moreover, Horna-Munoz et al. [66] observed the generation of vortical Kelvin–Helmholtz cells similar to those present at the interface between the forward and backward propagating currents in a classical temporally-evolving lock-exchange flow. Finally, similar to what was observed for confluences with moderate density stratification effects, the amount of mixed fluid inside the simulated port-confluence channel was by about 50% larger in the $Ri = 0.39$ simulations compared to the corresponding $Ri = 0$ simulation regardless of which tributary contained the denser fluid. In fact, the amount of mixed fluid in the two $Ri = 0.39$ simulations increased with respect to the $Ri = 0.04$ simulations, which indicates that the passage of lighter fluid above heavier fluid generates additional mixing inside the CHZ.

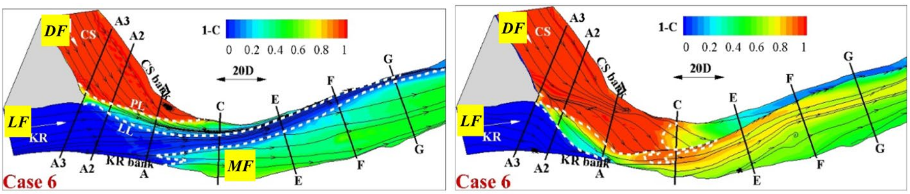


(a) (b)

**Fig. 19** KRCS simulations with strong density contrast. Mean nondimensional temperature, C, and 2–D streamline patterns in a simulation (Case 6) conducted with $VR = 0.65$, $Ri = 0.39$, $Fr_d = 1.6$. **a** C at free surface; **b** C near the bed. The two dashed lines correspond to $C = 0.1$ and $C = 0.9$. DF and LF denote the streams containing denser and, respectively, lighter fluid. MF denotes the large region of mixed fluid forming at the KR bank downstream of section A. Reproduced from Horna-Munoz et al. [66]

## 5 Mixing interface structure and stratification effects at discordant bed confluences

Numerical simulations performed for the ERSR confluence between the Ebro River (ER) and Segre River (SR) by Cheng and Constantinescu (23, 26) are used to describe flow hydrodynamics and mixing processes for a confluence with a highly discordant bed and to compare with processes described at concordant confluences. This confluence has made the object of several field studies (e.g., see Ramon et al., 2013, 2016). The ERSR confluence is asymmetric. The confluence angle is $110^0$ with the SR tributary being close to perpendicular to the post-confluence channel. The maximum flow depth in the Ebro River channel is about 1.6D, where D≈4 m is the average flow depth in the post-confluence channel which is characterized by a nonuniform flow depth with the channel being much deeper on the EB (South Bank) side of the cross section. The ratio between the flow depths in the two incoming channels in the simulations is 2.2–2.3, which is very close to values (1.8–2.2) observed at other confluences with a strong bed discordance [39],Guillén-Ludeña et al., 2015, 2016). The widths of the ER and SR tributaries are about 50D and 120D, respectively. Despite being shallower and transporting less discharge, the Segre River is much wider.

In a first series of simulations, the velocity ratio between the SR and ER tributaries was VR = 0.41, while the momentum ratio was MR = 0.075. Given that for those flow conditions, the difference between the temperatures of ER and SR tributaries was -4.3 $^0$C, simulations were performed with Ri = 0.65 ($Fr_d$ = 1.21) and Ri = 0 to be able to better understand stratification effects at this confluence. Additional simulations were performed by Cheng and Constantinescu (202b) with VR = 0.08, MR = 0.0032 and a temperature difference of + 2.7 °C, which corresponds to Ri = 0.89 and $Fr_d$ = 0.73. In the latter VR = 0.08 simulation, the low-momentum tributary contains the denser fluid, while the opposite is true for the VR = 0.41 simulations. Thus, in the two simulations with density contrast, the intrusions develop in opposite directions close to the free surface and the bed. The second difference is that MR is about 22 times smaller in the VR = 0.08, Ri = 1.89 simulation. Such conditions are close to the limiting case when a fast stream encounters a reservoir containing denser fluid. For such conditions, buoyancy effects play a major role in the way the two streams interact and mix starting at the confluence apex.

In the VR = 0.48 case with zero density contrast, the free-surface temperature distribution in an instantaneous flow field in Fig. 20a shows the presence of very large structures along the MI. One important finding of Cheng and Constantinescu [23] was that these vortical structures are not Kelvin–Helmholtz vortices that are expected to form given that VR is not close to unity. The structure of the MI was more similar to that of a MI in the wake-like mode where the larger structures formed via the interaction of the separated shear layers bordering the wake region. The large co-rotating structures observed at large distance from the confluence apex formed by the merging of the smaller vortices shed in the separated shear layer forming on the fast-speed side of the confluence apex. Moreover, there is no evidence of SOV cells forming near the MI. Such vortices are expected to form at a concordant bed confluence with similar planform geometry and velocity ratio, at least for negligible density contrast between the converging flows. There are also some similarities with what is generally observed at concordant bed confluences. The tilt of the MI was fairly negligible and the temperature distribution in the mean flow was fairly uniform along the vertical direction, with no mixed fluid being advected toward the channel banks (Fig. 20c).

The VR = 0.48, Ri = 0.67 case (Fig. 20b) is characterized by strong stratification effects. As opposed to the Ri = 0 case, no wake region forms. Rather, a large recirculating flow

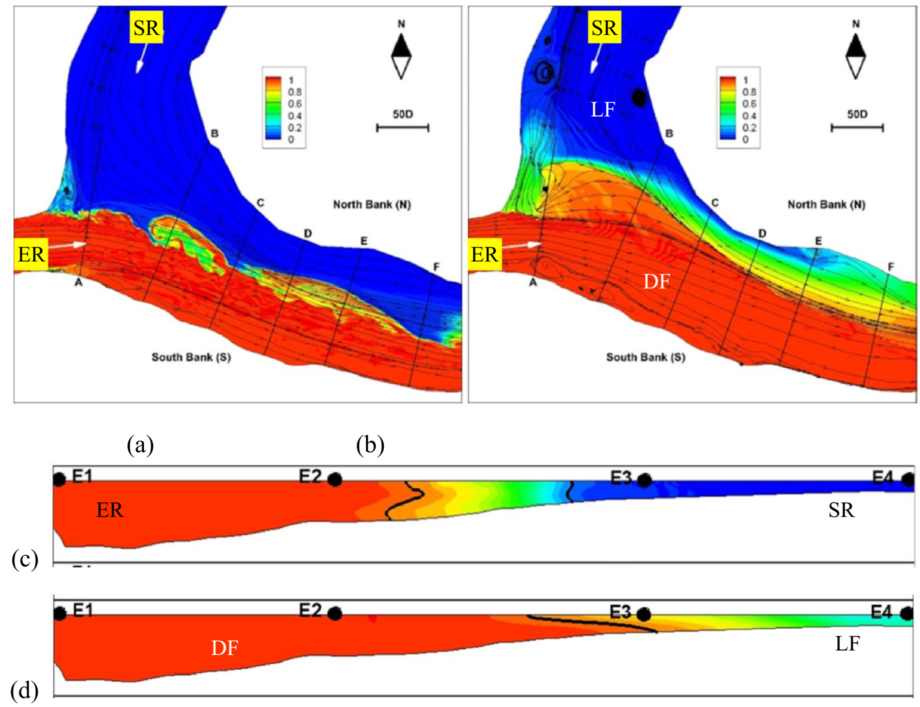


**Fig. 20** ERSR confluence between the Ebro River and Segre River. Simulations with and without density contrast. Visualization of mixing between the two streams in an instantaneous flow field using the non-dimensional temperature/density, C'. (**a**, **c**) VR = 0.48, Ri = 0; (**b**, **d**) VR = 0.48, Ri = 0.67, $Fr_d$ = 1.21. Also shown are 2D streamlines. Frames **a** and **b** show C' in a horizontal plane situated near the free surface. DF and LF denote the streams containing denser and, respectively, lighter fluid. Frames c and d show C' in section E. The solid black lines (C' = 0.1 and C' = 0.9) visualize the edges of the MI in the mean flow based. Reproduced from Cheng and Constantinescu [23]

eddy can be observed away from the junction apex. Its formation is mainly the result of the flow in the slower and wider SR tributary splitting into two components. Part of the SR flow follows the North bank line as it enters the post-confluence channel, while the remaining part moves toward the separated shear layer on the ER side of the confluence apex and then turns to allign with the flow originating in the high-speed tributary. Near the free surface, the MI is pushed toward the North bank starting very close to the confluence apex, something never observed at concordant confluences regardless of the density contrast. As opposed to the Ri = 0 case, there is no evidenve of the presence of larger-scale structures inside the MI. Consitent with the difference in density between the ER and SR tributaties, strong, near-bed intrusions of heavier fluid from the ER tributary penetrate into the SR side of the post-confluence channel. This also explains the high tilting of the MI on the Ebro River side (Fig. 20d).

Despite strong stratification effects, the lighter fluid from the Segre River tributary remains on the Segre side of the post-confluence channel in the VR = 0.48, Ri = 0.67 case (Fig. 20b). For concordant confluences, the flows containing heavier and lighter fluid were found to switch sides inside the post-confluence channel in simulations conducted with Ri = 0.39 (Fig. 19). Such a phenomenon which requires the presence of a two-layer flow structure was also observed at the ERSR confluence in a simulation conducted with VR = 0.08 and Ri = 1.89 simulation. As seen in Fig. 21b, after the heavier fluid from the SR plunges downwards, the core of higher density fluid moving near the bed reaches the opposite (South) bank just downstream of section A. Near the free surface (Fig. 21a), the core of lighter unmixed fluid originating in the Ebro River does not reach the North Bank. However, downstream of section D this free surface region containing unmixed fluid originating in the Ebro River is bordered on its both sides by mixed fluid originating in the Segre River, something impossible to happen in the absence of strong stratification effects. Another important observation is the in this simulation the MI cannot be considered to have the characteristics of a shallow mixing layer even at very small distances from the confluence apex. Finally, like in the corresponding Ri = 0 cases, no SOV cells formed in the Ri = 0.67 and Ri = 1.89 simulations. These results suggest that strong bed discordance may act toward suppressing the SOV cells regardless of the presence, or not, of density contrast between the incoming flows.

In terms of global rates of mixing, density contrast acted toward sharply increasing mixing in the VR = 0.08 simulations in which the denser fluid was situated in the low-discharge tributary. For example, the volume of well-mixed fluid was about 4 times larger in the Ri = 1.89 simulation compared to the Ri = 0 simulation at about 350D from the confluence apex. This result is also consistent with the findings of Ramon et al. (2014) who investigated mixing at the same confluence. An increase of mixing with increasing density difference between the incoming streams at discordant confluences was also observed by Lane et al. [81], though in their case the denser fluid was in the deeper tributary. However, a sharp increase of mixing with increasing density contrast should not be expected in all cases at confluences with a sharp bed discordance. For example, the volume of mixed fluid at 350D from the junction apex was about the same in the Ri = 0 and Ri = 0.67 simulations with VR = 0.41. Still, based on these examples one can conclude that in cases where density contrast is sufficiently large to induce strong flow stratification effects, one should not expect a decay of the overall rates of mixing with respect to the case where density contrast

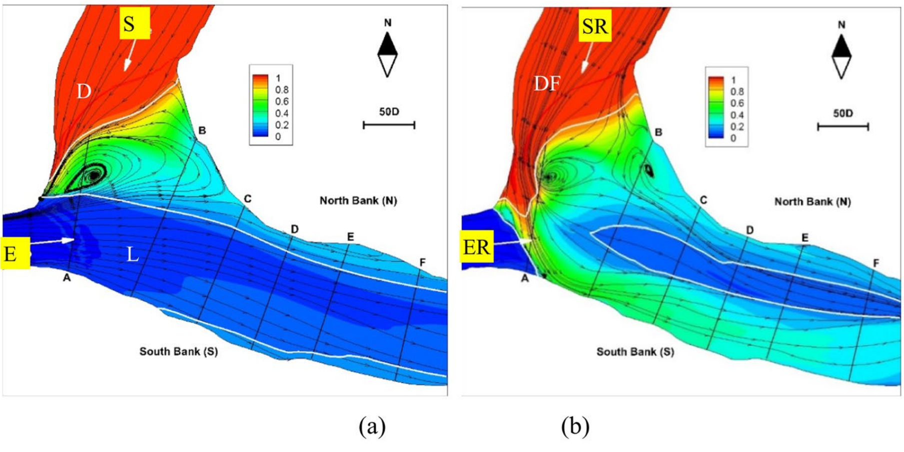


**Fig. 21** ERSR simulations with density contrast. Visualization of mixing between the two streams (VR = 0.08, Ri = 1.89, $Fr_d$ = 0.73) in the mean flow using the non-dimensional temperature field. **a** C' in a horizontal plane situated near the free surface. **b** C' in a deformed plane situated at about 0.1D from the bed surface. The white lines visualize the edges of the regions containing mixed fluid (C` = 0.1 and C` = 0.9) in the mean flow. Also shown are 2–D streamlines. Reproduced from Cheng and Constantinescu [26]

effects are negligible. We already pointed out that for strong bed discordance the analogy with a shallow mixing layer, that provides an excellent base for theoretical modeling for confluences with negligible and weak density contrast, cannot be used anymore. In some cases, a better analogy is that of a free surface jet entering a channel at one of its sides.

## 6 Bioenergetics metric at two large-size concordant bed confluences

The relationship between hydrodynamics and aquatic organisms' behaviour has made the object of numerous studies (e.g., see Triantafyllou et al., 2000 for a review). More recently, efforts were made to examine the importance of turbulence, vorticity, circulation, velocity gradients and kinetic energy gradients on the behavior of aquatic organisms [112],Lacey et al., 2012; Silva et al., 2013; Kerr et al., 2016; [156],Ligman et al., 2024). Velocity gradients in non-uniform flows are likely impacting fish and other aquatic organisms [12, 63]. Such velocity gradients are primarily located inside eddies and vortices with different orientations, inside cross stream cells of secondary flow, and inside flow separation and wake zones (Rempel et al., 1999; Abdi and Yasi, 2015; Tullos et al., 2016). Velocity gradients along with other micro-and meso-habitat parameters, such as river depth and width, are important factors for the specific stages of riverine species life cycles, e.g. spawning, substrate or larval refuges for salmonids and rheophilic cyprinids (Maddock, 1999; Muhar, 1996; Yang et al., 2008, Zhu et al., 2013). Fish are known to react to velocity patterns in high flows by adjusting their behaviors in spawning, feeding, and access to refugia (Rempel et al., 1999; Schwartz and Herricks, 2005). In most ecological systems, there is a positive correlation between biotic diversity and habitat heterogeneity (Bell et al., 1991), including heterogeneity of substrate and flow characteristics such as depth or velocity. This correlation is associated with the flow complexity within the stream [77]. In addition to flow structures, water environmental conditions also influence fish habitat preferences (Brown et al., 2004; Kramer, 1987). Despite previous studies have pointed out observed abundance and species richness downstream of river confluences [45, 46, 103], it is still unclear if and how the confluence hydrodynamics is related to those observed ecological patterns.

Two field surveys were conducted at the confluence between the Yangtze River and the Poyang Lake outflow channel to study fish density distribution using fish hydroacoustic detection, environmental DNA and acoustic velocity profiling. The discharge ratios of this confluence in the two surveys were similar, but the water quality conditions, represented by turbidity, differed greatly. The results demonstrated high spatial heterogeneity of fish density, size, and species near the confluence. In the Yangtze River, which is characterized by high flow velocity, the abundance of small-size fish was substantially higher than that in the Poyang Lake outflow channel, while large-sized fish chose their habitats more freely between the two tributaries and the post-confluence channel (Fig. 22). The convergence of two tributaries created prominent spatial heterogeneity of habitat conditions in the post-confluence channel. As a result, highest fish abundance and species biodiversity were observed downstream of the confluence apex. The species assemblage structure of the local fish community was also greatly affected by the change of water quality, e.g., the intrusion of a turbid flow from Poyang Lake into the Yangtze River.

Velocity gradients at the confluence between the Negro and Solimões Rivers were investigated in low (October 2014, FS – CNS1 survey) and relatively high flow conditions (April/May 2015, FS – CNS2 survey) using the bioenergetics metric $M_2$, which is defined as [34–36, 53]:

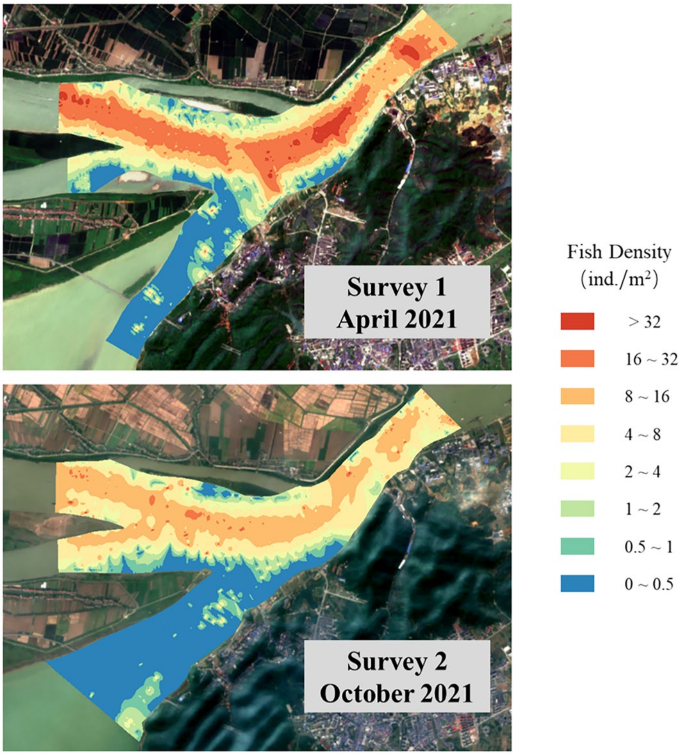


**Fig. 22** Map of fish density (ind./m.$^2$) around the confluence of the Yangtze River and the Poyang Lake outflow channel during Surveys 1 and 2. Reproduced from Yuan et al. [173]

$$M_2 = 2V_{avg}\frac{\left|\frac{V_2 - V_1}{\Delta s}\right|}{V_{\min}^2} \tag{1}$$

where, $V_2$ and $V_1$ are the depth-averaged velocity magnitudes, or the local cell-based velocity magnitudes, at points 1 and 2 separated by a distance $\Delta s$ along the direction in which the spatial change in the kinetic energy is computed, $V_{avg}$ is the average depth-averaged or cell-based velocity magnitude between points 1 and 2, $V_{min}$ is the minimum value between $V_2$ and $V_1$, and $s$ indicates the direction of the line passing through points 1 and 2. $M_2$ is proportional to the drag force acting on an organism and could represent the average amount of energy spent in moving from one location to another [34, 55]. It is scaled by the kinetic energy of the flow at the point of lower velocity, so it is indicative of the average rate of change in the kinetic energy per unit mass and unit length between two points [1/m].

The metric $M_2$ was first calculated using the transversal gradients of the depth-averaged velocity to identify the spatial distribution of $M_2$ within the confluence (2D analysis). The distance $\Delta s$ corresponded to the distance between two adjacent ADCP ensembles [55] and was close to 1 m. Then, $M_2$ was computed using the cell-based velocity. Both the transversal and vertical gradients of that velocity in the river cross-section were estimated to understand their distribution in the confluence region (3D analysis).

In this case, $\Delta s$ was the transversal or the vertical distance (about 1 m) between two adjacent ADCP cells [58]. Hence, it is expected that the 3D analysis based on the local velocity in a cell should be able to capture the average amount of energy spent by an organism while moving from one cell to another. Future studies should also consider the temporal fluctuations of the velocity which are experienced by the organisms living in the aquatic system (Lacey et al., 2012; [156],Ligman et al., 2024).

Figure 23 presents the map of the 2D $M_2$ metric. $M_2$ had large values at locations where the kinetic energy was low compared to the horizontal velocity gradient such as inside the Negro channel as well as inside the stagnation region, inside the flow separation region and near the mixing zone at the upstream section of the confluence. For high flow conditions, the metric $M_2$ peaked in an area approximately 800 m long and 300 m wide, starting 200 m downstream of the junction apex. This area was located over a bar dividing the two converging rivers (Fig. 23). The low flow had a larger shear zone due to lower minimum velocities, which increased the magnitude of the bioenergetics metric, $M_2$. This area of high $M_2$ values was located across the MI where larger velocity gradients and bed shear stresses were present.

The length of the region of high values of $M_2$ approximately corresponded to the realignment zone of the Negro and Solimões waters in the Amazon River channel. Inside this zone, large $M_2$ values were a consequence of the combined action of differences in streamwise velocity and rapid change in the flow direction. Another area of large $M_2$ values for both flow conditions corresponded to the separation region at the beginning of the Amazon channel, along its right bank, where a large decrease in the flow velocity was observed (Fig. 23). Intermediate $M_2$ values were observed along the riverbanks, even on the Negro River side. The lowest $M_2$ values were recorded in the central part of the Amazon channel, downstream of the mixing zone (Fig. 23).

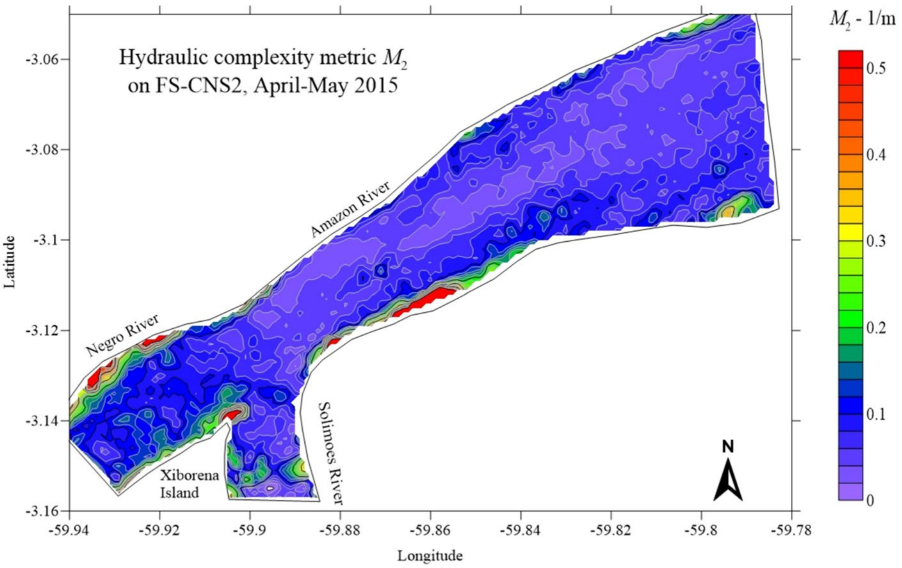


**Fig. 23** Map of depth-averaged $M_2$ metric at the confluence of the Negro and Solimões Rivers on April/May 2015 (FS-CNS2 survey). Reproduced from Gualtieri et al. [55]

The longitudinal distribution of $M_2$ from the 2D and 3D analyses for transects situated downstream of the junction for both flow conditions are compared in Fig. 24. Both the 2D and the 3D data show the peak values occurred immediately downstream of the junction apex, and these values decayed with the distance from the apex for both low (blue symbols) and relatively high (red symbols) flow conditions. A rapid decay was observed until approximately 4 to 5 km downstream of the confluence apex, corresponding to the central part of the CHZ. Farther downstream, in the region characterized by flow recovery, $M_2$ was almost constant. This region extended downstream of the last cross section where $M_2$ was estimated. These trends show that the patterns of spatial habitat correspond with the classic hydrodynamic features of a confluence.

The $M_2$ values from the 3D analysis were systematically larger than those estimated based on the 2D approach (Fig. 24). This difference was especially large inside the central part of the CHZ, where the medians estimated from the 3D and 2D approaches were 0.17 and 0.07, respectively. In between the central part of the CHZ and the end of the study area, the differences between the 3D and 2D approaches were smaller. In the 2D and 3D analyses, the $M_2$ values for low flow conditions were larger than those estimated for relatively high flow conditions. In the 3D analysis for low flow conditions, the $M_2$ computed values based on the velocity variation in the transverse direction were higher than those based on the vertical direction.

Nakajima et al. [111] investigated the density, biomass and distribution of meso-zooplankton and ichthyoplankton (fish larvae) communities around the Negro/Solimões confluence during the rainy season (March 2012). They found that meso-zooplankton density and biomass were higher in the black water of the Negro River compared to the muddy white water of the Amazon River. High concentration of ichtyoplankton were measured in the water column at a station located at the surface boundary between the two rivers, at the entrance of the Amazon channel. This station was close to the location of transect CNS2 during the FS – CNS1 and FS – CNS2 surveys (Fig. 13). Nakajima et al. [111] argued that this region may function as a boundary layer that offers benefits of both high food (zooplankton) concentrations from black water river and low predation risk from white water river. Gualtieri et al. [57] have found that, both at the water surface and at the bed, the

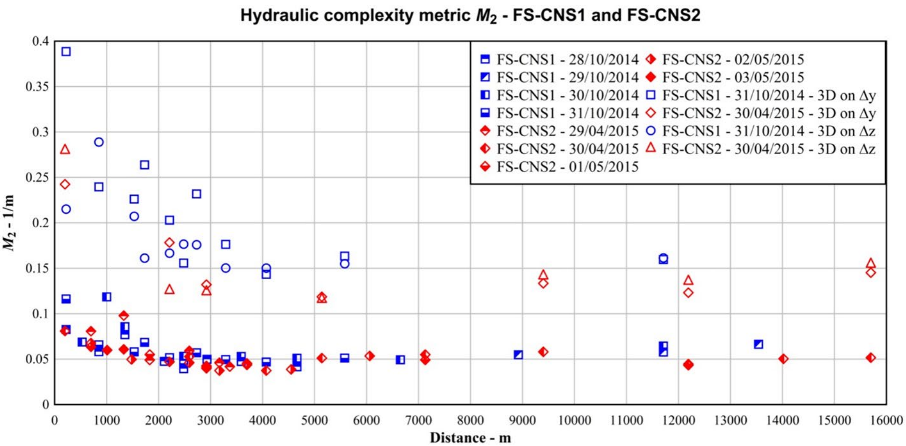


**Fig. 24** Longitudinal profile of $M_2$ at the confluence of the Negro and Solimões rivers for both surveys. Reproduced from Gualtieri et al. [58]

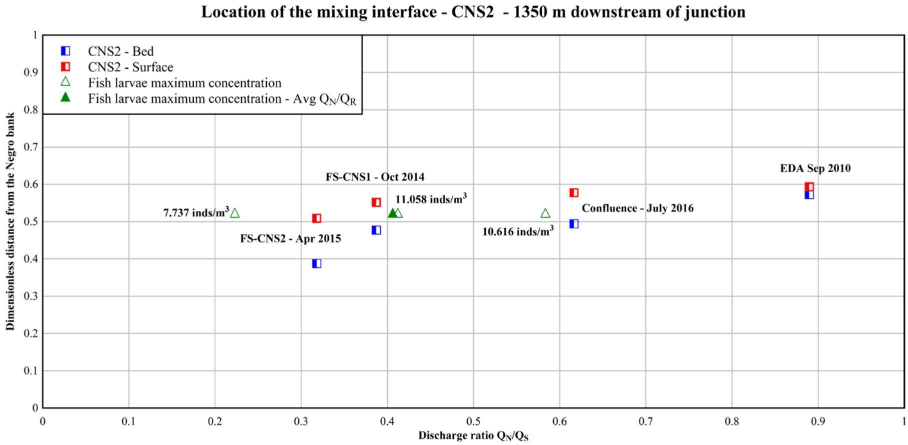


**Fig. 25** Dimensionless distance from the Negro bank vs discharge ratio $Q_R$ for the CNS2 survey. Reproduced from Gualtieri et al. [58]

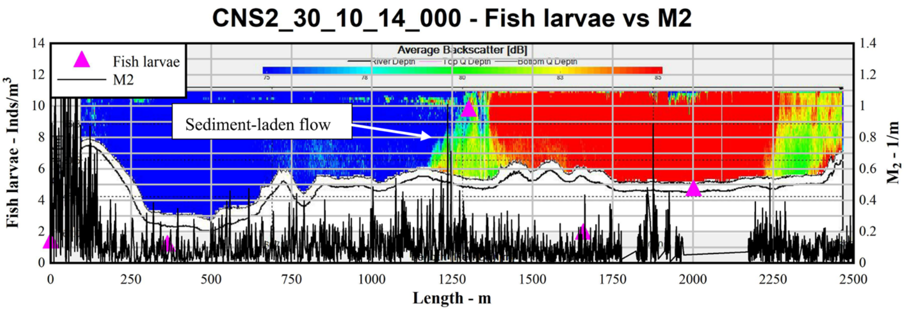


**Fig. 26** Distribution of backscatter intensity, $M_2$ metric and fish larvae concentration from survey CNS2 at the confluence of the Negro and Solimões Rivers. Reproduced from Gualtieri et al. [58]

distance between the MI and the Negro River riverbank correlated well with the discharge ratio between the Negro and Solimoes rivers, $Q_N/Q_S$ (Fig. 18a). As this ratio gets smaller, the distance decreased.

Figure 25 shows that on 3/10/2014, when the largest fish larvae concentration was measured, the location of Station 3 of Nakajima et al. [111] study closely corresponded with that of the MI at transect CNS2 on 30/10/2014 (Figs. 17 and 18a). In Fig. 26, the cross-sectional distribution of fish larvae concentration [111] was overlaid with the backscatter intensity data and the 2D spatial habitat metric $M_2$ at transect CNS2 (Fig. 13a) for low flow conditions. The peak of fish larvae concentrations (magenta triangle) was located within the inclined MI with the sediment-laden flow, where also the $M_2$ metric peaked. This analysis demonstrates that the $M_2$ metric can be used to identify hot spots of aquatic species richness.

While it is widely acknowledged that river confluences have important ecological and morphological functions, the relationship between confluence hydrodynamics and aquatic organisms' behaviour needs further investigation. Aquatic organisms are subjected to hydro-environmental and ecological conditions which can change in space and time during their active or passive motion within the confluence. Past laboratory studies have already pointed out the role of turbulence on organisms' behavior [112],Lacey et al., 2012; [156]. Hence, future field studies should adapt their instrumentation and measurement methodology to be able to capture the response of the organisms to any change in those conditions.

## 7 Application of remotely sensed techniques in confluences field studies

Various remotely sensed image-based techniques and methods were developed in the last decades to acquire information about river spatial objects and processes without any physical contact. They include several types of sensors, such as digital cameras, video cameras, thermal-, infra-red-, hyper- and multi-spectral sensors, light detection and ranging (LiDAR), ground-penetrating radar (GPR) or geophones. They could be mounted on platforms, such as satellite, airborne, unmanned aerial vehicles (UAVs) or even positioned on the ground [116]. Their application to river confluences mainly focused on three objectives: the identification of confluence planform temporal evolution, the analysis of TSS dynamics in the post-confluence channel and the analysis of the surface flow structure inside the CHZ (Table 1).

Most studies investigated the spatial mobility of river confluences due to hydrodynamics and morphodynamics processes [41, 51, 74, 83],Mriganka and Saikatm 2023; [121, 171] and the TSS surface dynamics and mixing inside the post-confluence channel [22, 68,

**Table 1** – Remotely sensed image-based studies of river confluences

| Reference | Confluence | Objective | Technique |
|---|---|---|---|
| Islam et al. [68] | Ganges/Brahmaputra | TSS dynamics | LANDSAT |
| Park and Latrubesse [114] | Negro/Solimões | TSS dynamics | MODIS |
| Dixon et al. [41] | – | Planform evolution | LANDSAT |
| Umar et al. [157] | Missouri/Mississippi | TSS dynamics | LANDSAT |
| Marinho et al. [101] | Negro/Solimões | TSS dynamics | MODIS |
| Figueiredo et al. (2019) | Sinos River Basin | Junction angle | Google Earth Pro / UAV |
| Lewis et al. (2018a) | Illinois rivers | 2D flow structure | LSPIV / UAV |
| Lewis et al. (2018b) | Illinois rivers | 2D flow structure | LSPIV / UAV |
| Gazi et al. [51] | Ganges–Brahmaputra–Meghna system | Planform evolution | LANDSAT |
| Chalov et al. [22] | Aldan/Lena | TSS dynamics | LANDSAT |
| Sabrina et al. [138] | Saline branch | Surficial flow structure | LSPIV |
| Mohsen et al. [108] | Maros/Tisza | TSS dynamics | SENTINEL-2 |
| 42, 43) | Neigette/Mitis | Surficial flow structure | UAV |
| 170, 171, 172) | Nihong/Yarlung Zangbo | Planform evolution | LANDSAT |
| Khan et al. [74] | Ganges/Jamuna/Padma | Planform evolution | LANDSAT |
| Kwon et al. [78] | Hwang/Nakdong | TSS dynamics | UAV |
| Lawal and Omosanya [83] | Benue/Niger | Planform evolution | LANDSAT |
| Mriganka and Saikat [110] | Brahmaputra | Planform evolution | LANDSAT |
| Raj and Singh [121] | Kosi/Ganga | Planform evolution | LANDSAT |

78, 101, 108, 114, 157] using remotely sensed images collected over decades from different satellites, such as LANDSAT, MODIS and SENTINEL-2, and UAVs.

Dixon et al. [41] used a 40-year record of Landsat Imagery to elucidate the rates of change and areal extent over which 14 confluences situated on large rivers, such as Amazon, Orinoco, Congo and Yangtze, may migrate. They found that the potential areal extent of confluence-induced morphodynamics changes is much greater than previously assumed. Extensive migration of the confluence location was more common than currently assumed with confluence mobility often tied to the lithological and hydrological characteristics of the drainage basins that determine the sediment yield. Yuan et al. [171] used georeferenced Landsat imagery spanning the period 1986–2020 (of dry season) to analyze the historical evolution of the planform geometry of the large multi-channel confluence between the Yarlung Zangbo River (YZR) and the anabranching Niyang River (NR). The confluence is located on the longest plateau river in China. The YZR is one of the world's high-altitude rivers (basin area $=24.6\times10^4$ $km^2$) while the NR is one of its major tributaries. Representative images from five different time periods (1986, 1993, 2000, 2010, 2020) were selected for analysis (Fig. 27).

The analysis was focused on a 30 km reach of the YZR located upstream and downstream of the confluence between the NR and the YZR. The study revealed that the interaction between the multi-channel NR tributary on the left side and the mountain on the right side created a stable confluence planform as compared to the upstream and downstream reaches of the YZR, which suffered from sandbar migration, meandering and a head-cut. Upstream of the confluence, a sandbar was found to slowly move downstream, and sediment was deposited near the first sub-confluence, reducing the confluence angle from $120^{\circ}$ to $85^{\circ}$. Downstream of the confluence, a natural curve cut-off occurred. After 2010, the sandbars were gradually covered by vegetation, which restrained the channel evolution. Both studies fully demonstrated that the application of about five decades of global imagery provides a great tool to study the morphodynamics of large river confluences over decadal timescales.

Park and Latrubesse [114] applied MODIS imagery to characterize the spatio-temporal patterns of TSS transport in the Negro/Solimões confluence during 2005 (drought), 2007 and 2009 (flood) by mapping the surface water distribution. They found that surface water mixing depends on the hydrological season, with the highest mixed-homogenized area observed during water discharge peak season and the lowest during water discharge rising season. The degree of water mixture also depended on the yearly hydrological regime with the highest rates of water mixing occurring in 2009, followed by 2005 and 2007. Kwon et al. [78] investigated mixing of TSS at the confluence of the Hwang River and Nakdong River in South Korea by analyzing the TSS spectral characteristics from high-resolution hyperspectral data collected by an UAV-mounted camera. The study demonstrated the advantages of using the hyperspectral approach for investigating TSS mixing in river confluences. High-resolution hyperspectral imagery-based TSS measurements provide a substantial supplement when high-resolution TSS data are required, such as at river confluences and in meandering streams. These studies demonstrated that compared with traditional methods based on water sampling, remote sensing-based TSS measurement methods can be an ideal way to obtain high-resolution data to analyse mixing dynamics over large spatio-temporal scales in a complex river system. The main limitation is that such methods can measure only the near-surface concentration [78, 114].

Relatively few remotely sensed studies focused on investigating flow structure at river confluences [42, 43],Lewis et al., 2018a, 2018b; [138]. Lewis et al. (2018a, 2018b) estimated the accuracy of small UAV-based LSPIV for measuring 2D mean surface velocities

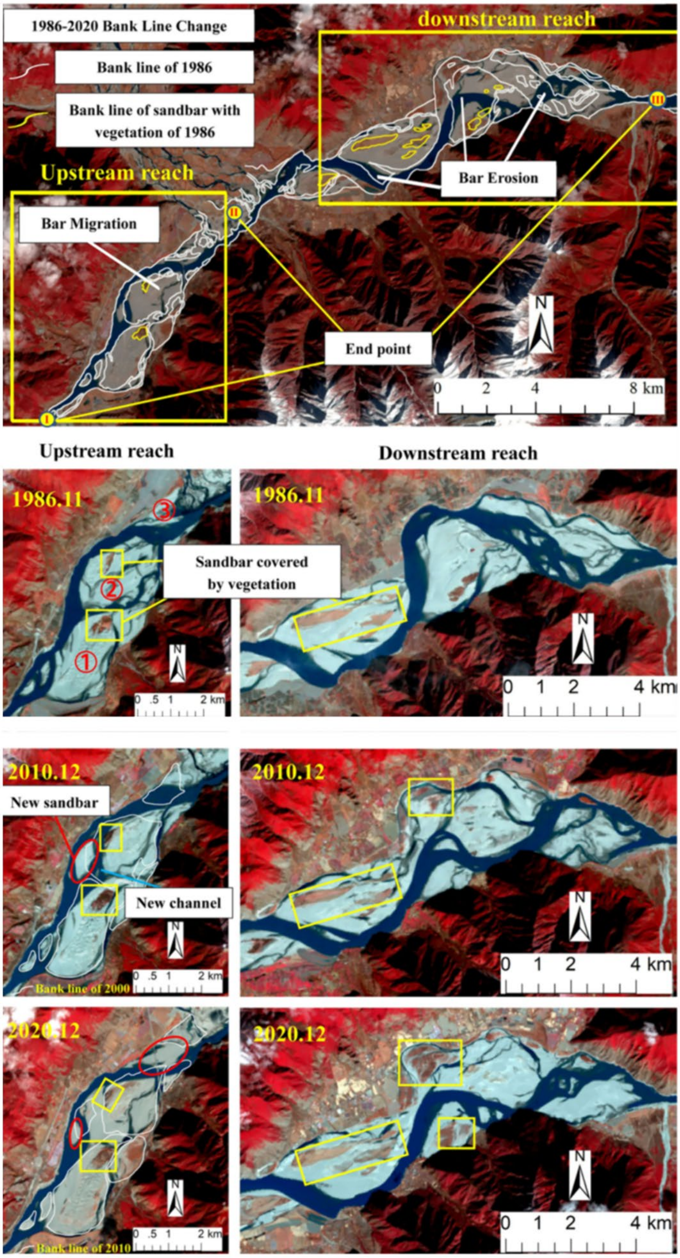


**Fig. 27** Landsat image sequence showing planform changes near the confluence of the Yarlung Zangbo River (YZR) and Niyang River (NR). The outlet of the first stream of the NR and the angle shift over time with the erosion and deposition of sandbar. Sandbars covered by vegetation are marked by the yellow frames. (The background of the first picture is from 2020. [170–172] Reproduced from Yuan et al. [171]

and quasi-instantaneous 2D velocities obtained from successive image frames at two small stream confluences in east-central Illinois, USA. They compared UAV-based LSPIV measurements with those from a stationary camera and an ADV. They found that UAV-based LSPIV can provide accurate, high-resolution measurements of mean surface velocities over large spatial areas of persistent 2D flow and can characterize evolving 2D flow structures. The method can also be used to characterize the structure of turbulent vortices within the MI under appropriate conditions.

Sabrina et al. [138] applied LSPIV to map two-dimensional flow structure at the water surface of a small confluence in East Illinois and to examine variation in the flow structure over time. Their study demonstrated that the low cost of equipment, seeding material, setup, and the analysis of the LSPIV data should allow for investigating flow structure at river confluences over larger spatial domains using multiple fixed-mount cameras. Duguay et al. [42] collected aerial drone videos of the small-scale confluence between the Neigette and the Mitis rivers to investigate MI dynamics. They also conducted particle tracking velocimetry (PTV) measurements over a region of the MI. Duguay et al. [43] used drone imagery of coherent structures in the mixing zone between the turbid Coaticook River and the clear-water Massawippi River. The above studies fully demonstrate the large potential of remote sensing techniques to improve our current knowledge and understanding of confluence hydrodynamics and morphodynamics.

## 8 Conclusions and future research on flow and processes at river confluences

The knowledge of hydrodynamics, morphodynamics and ecological features of river confluences has been dramatically improved over the last three decades thanks to a large amount of laboratory, field and numerical studies. These studies clarified many aspects related to the multiple roles played by the streamwise oriented vortical (SOV) cells forming in the vicinity of the mixing interface (MI) and showed that density contrast effects are much more important than previously thought. In addition, these studies have confirmed that river confluences are hot spots for aquatic ecology, highlighted several multimedia processes at river confluences (gas-transfer, hyporheic fluxes) and demonstrated the large potential of remotely sensed methods in revealing key aspects of river confluences. Nevertheless, further research is still needed to better clarify several aspects related to river confluences and future efforts should focus on addressing the following phenomena and research challenges:

- Field studies, especially in large rivers confluences, should focus on the complex interaction among hydrodynamics, morphodynamics and ecological features. Hence, they should be carried out using a combination of hydro-acoustic, seismic, water chemistry, fish detection and remote-sensing methods.
- The exchange between surface water and groundwater at a river confluence needs to be extensively investigated. Experimental and numerical studies can provide critical information on the hyporheic fluxes.
- Investigations of the interactions between hydrodynamics and organisms' behaviour at a river confluence need to be carried out using field instrumentation and measurement methodologies that can capture the response of the organisms to relevant changes in the hydro-environmental and ecological conditions within the aquatic system.

- The effects of floodplain vegetation and migrating bedforms on confluence hydrodynamics need to be experimentally and numerically investigated.
- Multidisciplinary investigations of biological and ecological aspects related to fish sheltering, contaminants' mixing, gas-transfer, total dissolved gas (TDG), wood/woody debris accumulation and transport at river confluences are needed.
- Development of numerical models that can accurately predict sediment transport and morphodynamics at confluences including the formation and evolution of the confluence scour hole. This may require flow solvers using eddy resolving techniques rather than unsteady RANS and novel methods to couple the bed hydrodynamics module with the flow solver module.
- At larger scales, anabranching large rivers are characterized by diffluence-confluence units associated to mid channel bar and islands. Their hydrodynamics and morphodynamics needs to be investigated using field, numerical and remote sensing techniques.
- At the basin scale, the multidecadal changes in river connectivity related to the evolution of confluences planform are still poorly understood. Further studies mainly based on remote sensing methods are needed.

**Acknowledgements** George Constantinescu acknowledges the cooperative research carried out with many collaborators including Alexander Sukhodolov, Bruce Rhoads, Zhengyang Cheng, Daniel Horna-Munoz, Shin Miyawaki, Chenyu Jiang, Quinn Lewis and Saiyu Yuan. Carlo Gualtieri acknowledges the cooperative research carried out on river confluences in the last decade with several colleagues from different countries, such as Marco Ianniruberto, Naziano Filizola, Theodore Endreny, Hongwu Tang, Saiyu Yuan.

**Author Contribution** Both authors equally contributed to writing this manuscript.

**Funding** No funding was received to assist with the preparation of this manuscript.

**Data availability** No datasets were generated or analysed during the current study.

## Declarations

**Competing interests** The authors declare no competing interests.

## References

1. Ashmore PE (1982) Laboratory modelling of gravel braided stream morphology. Earth Surf Proc Land 7(3):201–225. https://doi.org/10.1002/esp.3290070301
2. Ashmore P, Parker G (1983) Confluence scour in coarse braided streams. Wat Resour Res 19:392–402
3. Ashmore PE, Ferguson RI, Prestegaard KL, Ashworth PJ, Paola C (1992) Secondary flow in anabranch confluences of a braided, gravel-bed stream. Earth Surf Proc Land 17:299–311
4. Bahmanpouri F, Barbetta S, Gualtieri C, Ianniruberto M, Filizola N, Termini D, Moramarco T (2022) Prediction of river discharges at confluences based on Entropy theory and surface-velocity measurements. J Hydrol. https://doi.org/10.1016/j.jhydrol.2021.127404
5. Benda L, Poff LN, Miller D, Dunne T, Reeves G, Pess G, Pollock M (2004) The network dynamics hypothesis: how channel networks structure riverine habitats. Bioscience 54(5):413
6. Best JL, Reid I (1984) Separation zone at open-channel junctions. J Hydraul Eng 110(11):1588–1594. https://doi.org/10.1061/(ASCE)0733-9429(1984)110:11(1588)
7. Best J.L. (1987). Flow dynamics at river channel confluences: Implications for sediment transport and bed morphology. Recent Developments in Fluvial Sedimentology, Frank G.Ethridge, Romeo M.Flores, Michael D. Harvey
8. Best JL (1988) Sediment transport and bed morphology at river channel confluences. Sedimentology 35(3):481–498. https://doi.org/10.1111/j.1365-3091.1988.tb00999.x

9. Best JL, Roy AG (1991) Mixing-layer distortion at the confluence of channels of different depth. Nature 350:411–413. https://doi.org/10.1038/350411a0
10. Best JL, Ashworth PJ (1997) Scour in large braided rivers and the recognition of sequence stratigraphic boundaries. Nature 387:275–277
11. Best, J.L., Parsons, D., Kellman, P., Amsler, M., Szupiany, R., Kostaschuck, R., Lane, S., Hardy, R., Orfeo, O. (2007), On the influence of density contrasts between mixing flows at channel confluences: the Río Bermejo and Río Paraguay, Argentina. Workshop on Morphodynamic Processes in Large Lowland Rivers, Santa Fe, Argentina, November 2007
12. Biggs BJF, Duncan MJ, Francoeur SN, Meyer WD (1997) Physical characterisation of microform bed cluster refugia in 12 headwater streams, New Zealand. NZ J Mar Freshwat Res 31(4):413–422
13. Biron PM, Roy AG, Best JL, Boyer CJ (1993) Bed morphology and sedimentology at the confluence of unequal depth channels. Geomorphology 8:115–129
14. Biron PM, Roy AG, Best JL (1996) Turbulent flow structure at concordant and discordant open-channel confluences. Exp Fluids 21(6):437–446. https://doi.org/10.1007/BF00189046
15. Boddy NC, Booker DJ, McIntosh AR (2020) Heterogeneity in flow disturbance around river confluences influences spatial patterns in native and non-native species co-occurrence. Biol Invasions 22:3457–3475. https://doi.org/10.1007/s10530-020-02334-1
16. Bouchez J, Lajeunesse E, Gaillardet J, France Lanord C, Dutra Maia P, Maurice L (2010) Turbulent mixing in the Amazon River: The isotopic memory of confluences. Earth Planet Sci Lett 290:37–43
17. Bowes RE, Bergman E, Donadi S, Greenberg L, Sandin L, Lind L (2023) Landscape features control river's confluences water quality and tributary fish composition. River Res Appl 39(6):1025–1036. https://doi.org/10.1002/rra.4133
18. Boyer CJ, Roy AG, Nest JL (2006) Dynamics of a river channel confluence with discordant beds: flow turbulence, bed load sediment transport, and bed morphology. J Geophys Res 111:F04007
19. Bradbrook KF, Biron PM, Lane SN, Richards KS, Roy AG (1998) Investigation of controls on secondary circulation in a simple confluence geometry using a three-dimensional numerical model. Hydrol Process 12(8):1371–1396
20. Bradbrook KF, Lane SN, Richards KS (2000) Numerical simulation of three-dimensional, time-averaged flow structure at river channel confluences. Water Resour Res 36(9):2731–2746. https://doi.org/10.1029/2000WR900011
21. Bradbrook KF, Lane SN, Richards KS, Biron PM, Roy AG (2001) Role of bed discordance at asymmetrical river confluences. J Hydraul Eng 127:351–368
22. Chalov SR, Tarasov MK, Chalova AS (2021) The Patterns of Seasonality of the Suspended Sediment Load along the Braided Channel of the Lena River. Geogr Nat Resour 42:353–360. https://doi.org/10.1134/S1875372821040041
23. Cheng Z, Constantinescu G (2018) Stratification effects on flow hydrodynamics and mixing at a confluence with a highly discordant bed and a relatively low velocity ratio. Water Resour Res 54:4537–4562. https://doi.org/10.1029/2017WR022292
24. Cheng D, Song J, Wang W, Zhang G (2019) Influences of riverbed morphology on patterns and magnitudes of hyporheic water exchange within a natural river confluence. J Hydrol 574:75–84
25. Cheng Z, Constantinescu G (2020) Near-field and far-field structure of shallow mixing layers. J Fluid Mech 904:A21. https://doi.org/10.1017/jfm.2020.638
26. Cheng Z, Constantinescu G (2020) Stratification effects on hydrodynamics and mixing at a river confluence with discordant bed. Environ Fluid Mech 20:843–872. https://doi.org/10.1007/s10652-019-09725-6
27. Cheng Z, Constantinescu G (2021) Shallow mixing layers between non-parallel streams in a flat-bed wide channel. J Fluid Mech 916:A41. https://doi.org/10.1017/jfm.2021.254
28. Cheng Z, Constantinescu G (2022) Shallow mixing interfaces between parallell streams of unequal densities. J Fluid Mech 945:A2. https://doi.org/10.1017/jfm.2022.505
29. Constantinescu G (2014) LE of shallow mixing interfaces: A review. Environ Fluid Mech 14:971–996. https://doi.org/10.1007/s10652-013-9303-6
30. Constantinescu G, Miyawaki S, Rhoads B, Sukhodolov A, Kirkil G (2011) Structure of turbulent flow at a river confluence with momentum and velocity ratios close to 1: Insight provided by an eddy-resolving numerical simulation. Water Resour Res 47(5):W05507. https://doi.org/10.1029/2010WR010018
31. Constantinescu G, Miyawaki S, Rhoads BL, Sukhodolov AN (2012) Numerical analysis of the effect of momentum ratio on the dynamics and sediment entrainment capacity of coherent flow structures at a stream confluence. J Geophysical Research: Earth Surface 117:F04028. https://doi.org/10.1029/2012JF002452

32. Constantinescu G, Miyawaki S, Rhoads BL, Sukhodolov AN (2014) Numerical evaluation of the effects of planform geometry and inflow conditions on flow, turbulence structure, and bed shear velocity at a stream confluence with a concordant bed. J Geophysical Research: Earth Surface 119:2079–2097. https://doi.org/10.1002/2014JF003244
33. Constantinescu G, Miyawaki S, Rhoads B, Sukhodolov A (2016) Influence of planform geometry and momentum ratio on thermal mixing at a stream confluence with a concordant bed. Environ Fluid Mech 16(4):845–873. https://doi.org/10.1007/s10652-016-9457-0
34. Crowder DW, Diplas P (2000) Evaluating spatially explicit metrics of stream energy gradients using hydrodynamic model simulations. Can J Fish Aquat Sci 57(7):1497–1507
35. Crowder DW, Diplas P (2002) Vorticity and circulation: spatial metrics for evaluating flow complexity in stream habitats. Can J Fish Aquat Sci 59(4):633–645
36. Crowder DW, Diplas P (2006) Applying spatial hydraulic principles to quantify stream habitat. River Res Appl 22(1):79–89
37. Cushman-Roisin, B., Gualtieri, C., Mihailovic, D.T. (2008). Environmental fluid mechanics: Current issues and future outlook. In *Fluid Mechanics of Environmental Interfaces*, 1st ed.; Gualtieri, C., Mihailović, D.T., Eds.; Taylor & Francis, London, UK, 3–17
38. Cushman-Roisin B, Constantinescu G (2019) Dynamical adjustment of two streams past their confluence. J Hydraul Res 58(2):305–313. https://doi.org/10.1080/00221686.2019.1573765
39. De Serres B, Roy AG, Biron PM, Best JL (1999) Three-dimensional structure of flow at a confluence of river channels with discordant beds. Geomorphology 26(4):313–335. https://doi.org/10.1016/S0169-555X(98)00064-6
40. Ding R, Zhang X, Chen M, Lian Y, Yu D (2023) Vorticity preference of the Yangtze finless porpoise (Neophocaena asiaeorientalis) during the dry season at the Wanhe River Estuary confluence. Ecol Model 485:110504. https://doi.org/10.1016/j.ecolmodel.2023.110504
41. Dixon SJ, Sambrook Smith GH, Best JL, Nicholas AP, Bull JM, Vardy ME, Sarker MH, Goodbred S (2018) The planform mobility of river channel confluences: Insights from analysis of remotely sensed imagery. Earth-Sci Rev 176:1–18. https://doi.org/10.1016/j.earscirev.2017.09.009
42. Duguay J, Biron P, Buffin-Bélanger T (2022) Large-scale turbulent mixing at a mesoscale confluence assessed through drone imagery and eddy-resolved modelling. Earth Surf Proc Land 47(1):345–363
43. Duguay J, Biron PM, Lacey J (2022) Aerial observations and numerical simulations confirm density-driven streamwise vortices at a river confluence. Water Resources. Research 58(7):e2021WR031527
44. Duguay J, Biron PM, Lacey J (2022) Impact of density gradients on secondary flow of a river confluence. Water Resources Research. 58:e2022WR032720
45. Farjalla VF (2014) Are the mixing zones between aquatic ecosystems hot spots of bacterial production in the Amazon River system? Hydrobiologia 728:153–165
46. Fernandes CC, Podos J, Lundberg GJ (2004) Amazonian Ecology: Tributaries Enhance The Diversity of Eletric Fishes. Science 305:1960–1962
47. Figueiredo Pereira M, Lippo Barbieiro B, Carneiro M, Kobiyama M (2019) Determination of the junction angle in fluvial channels from georeferenced aerial images from Google Earth Pro and UAV. Ambiente & Água - An Interdisciplinary Journal of Applied Science 14:5. https://doi.org/10.4136/ambi-agua.2345
48. Fingert E, Krylenko I, Belikov V, Golovlyov P, Zavadskii A, Samokhin M (2019) Two-dimensional hydrodynamic modelling of channel processes and floods characteristics at the confluence of the Amur and Zeya rivers. Proc IAHS 381:73–77. https://doi.org/10.5194/piahs-381-73-2019
49. Fraser DF, Gilliam JF, Yip-Hoi T (1995) Predation as an Agent of Population Fragmentation in a Tropical Watershed. Ecology 76(5):1461–1472
50. Gaudet JM, Roy AG (1995) Effect of bed morphology on flow mixing length at river confluences. Nature 373:138–139
51. Gazi MY, Roy H, Mia MB et al (2020) Assessment of Morpho-Dynamics through Geospatial Techniques within the Padma-Meghna and Ganges-Jamuna River Confluences, Bangladesh. *KN* -. J Cartography and Geographic Information 70:127–139. https://doi.org/10.1007/s42489-020-00051-2
52. Ghostine R, Vazquez J, Tefous A, Mose R, Ghenaim A (2012) Comparative study of 1D and 2D flow simulations at open-channel junctions. J Hydraul Res 50(2):164–170
53. Golpira A, Baki ABM, Ghamry H, Katopodis C, Withers J, Minkoff D (2022) An experimental study: effects of boulder placement on hydraulic metrics of instream habitat complexity. Sci Rep 12:13156. https://doi.org/10.1038/s41598-022-17281-1
54. Gualtieri, C., Pulci Doria, G. (2008), Gas-transfer at unsheared free-surfaces, in *Fluid Mechanics of Environmental Interfaces*, 131–161, https://doi.org/10.4324/9780203895351-13
55. Gualtieri C, Ianniruberto M, Filizola N, Santos R, Endreny T (2017) Hydraulic complexity at a large river confluence in the Amazon basin. Ecohydrology 10(7):e1863

56. Gualtieri, C., Filizola, N., de Oliveira, M., Santos, A. M., Ianniruberto, M. (2018). A field study of the confluence between Negro and Solimões Rivers Part 1: Hydrodynamics and sediment transport. *Comptes Rendus Geoscience*. 350(1–2) 31–42
57. Gualtieri C, Ianniruberto M, Filizola, (2019) On the mixing of rivers with a difference in density: the case of the Negro/Solimões confluence. Brazil. Journal of Hydrology 578(11):124029
58. Gualtieri C, Abdi R, Ianniruberto M, Filizola N, Endreny T (2020) A 3D analysis of spatial habitat metrics about the confluence of Negro and Solimões Rivers Brazil. Ecohydrology. https://doi.org/10.1002/eco.2166
59. Gualtieri C, Martone I, Filizola N, Ianniruberto M (2020) Bedform Morphology in the Area of the Confluence of the Negro and Solimões-Amazon Rivers. Brazil Water 12(6):1630. https://doi.org/10.3390/w12061630
60. Gualtieri, C., Ianniruberto, M. (2023). A field study about a diffluence-confluence unit in Amazon River. *XL IAHR Congress*, Vienna, Austria, August 21/25, 2023
61. Guillén-Ludeña S, Franca MJ, Cardoso AH, Schleiss AJ (2016) Evolution of the hydromorphodynamics of mountain river confluences for varying discharge ratios and junction angles. Geomorphology 255:1–15. https://doi.org/10.1016/j.geomorph.2015.12.006
62. Guillem Ludena S, Cheng Z, Constantinescu G, Franca MJ (2017) Hydrodynamics of mountain river confluences and its relationship to sediment transport. J Geophysical Research: Earth Surface. https://doi.org/10.1002/2016JF0044122
63. Hayes JW, Jowett IG (1994) Microhabitat models of large drift-feeding Brown Trout in three New Zealand rivers. North Am J Fish Manag 14:710–725
64. Herrero H, Garcia MC, Pedocchi F, Lopez G, Szupiany RN, Piacenza C (2016) Flow structure at a confluence: experimental data and the bluff body analogy. J Hydraul Res 54(3):263–274
65. Herrero HS, Lozada JMD, Garcia CM, Szupiany RN, Best J, Pagot M (2018) The influence of tributary flow density differences on the hydrodynamic behavior of a confluent meander bend and implications for flow mixing. Geomorphology 304:99–112
66. Horna-Munoz D, Constantinescu G, Rhoads B, Lewis Q, Sukhodolov A (2020) Density effects at a concordant bed natural river confluence. Water Resources Research. https://doi.org/10.1029/2019WR026217
67. Ianniruberto M, Trevethan M, Pinheiro A, Andrade JF, Dantas E, Filizola N, Santos A, Gualtieri C (2018) A field study of the confluence between Negro and Solimões Rivers Part 2: River bed morphology and stratigraphy. Comptes Rendus Geoscience 350(1–2):43–54
68. Islam MR, Yamaguchi Y, Ogawa K (2001) Suspended sediment in the Ganges and Brahmaputra Rivers in Bangladesh: observation from TM and AVHRR data. Hydrol Process 15:493–509. https://doi.org/10.1002/hyp.165
69. Ismail H, Viparelli E, Imran J (2016) Confluence of density currents over an erodible bed. J Geophys Res Earth Surf 121(7):1251–1272. https://doi.org/10.1002/2015JF003768
70. Jiang C, Constantinescu G, Yuan S, Tang H (2023) Flow hydrodynamics, density contrast effects and mixing at the confluence between the Yangtze River and the Poyang Lake channel. Environ Fluid Mech 23:229–257. https://doi.org/10.1007/s10652-022-09848-3
71. Kenworthy ST, Rhoads BL (1995) Hydrologic control of spatial patterns of suspended sediment concentration at a stream confluence. J Hydrol 168(1–4):251–263. https://doi.org/10.1016/0022-1694(94)02644-Q
72. Keylock CJ, Hardy RJ, Parsons DR, Ferguson RI, Lane SN, Richards KS (2005) The theoretical foundations and potential for large-eddy simulation (LES) in fluvial geomorphic and sedimentological research. Earth Sci Rev 71:271–301
73. Keylock CJ, Constantinescu G, Hardy RJ (2012) The application of computational fluid dynamics to natural river channels: Eddy resolving versus mean flow approaches. Geomorphology 179:1–20. https://doi.org/10.1016/j.geomorph.2012.09.006
74. Khan NS, Roy SK, Mazumder MTR et al (2022) Assessing the long-term planform dynamics of Ganges-Jamuna confluence with the aid of remote sensing and GIS. Nat Hazards 114:883–906. https://doi.org/10.1007/s11069-022-05416-6
75. Kiffney PM, Greene CM, Hall JE, Davies JR (2006) Tributary streams create spatial discontinuities in habitat, biological productivity, and diversity in mainstem rivers. Can J Fish Aquat Sci 63(11):2518–2530
76. Konsoer K, Rhoads B (2014) Spatial–temporal structure of mixing interface turbulence at two large river confluences. Environ Fluid Mech 14(5):1043–1070
77. Kozarek JL, Hession WC, Dolloff CA, Diplas P (2010) Hydraulic Complexity Metrics for Evaluating In-Stream Brook Trout Habitat. J Hydraul Eng 136(12):1067–1076

78. Kwon S, Won Seo I, Lyu S (2023) Investigating mixing patterns of suspended sediment in a river confluence using high-resolution hyperspectral imagery. Journal of Hydrology. https://doi.org/10.1016/j.jhydrol.2023.129505
79. Lambs L (2004) Interactions between groundwater and surface water at river banks and the confluence of rivers. J Hydrol 288(3–4):312–326. https://doi.org/10.1016/j.jhydrol.2003.10.013
80. Lane SN, Bradbrook KF, Richards KF, Biron PM, Roy AG (2000) Secondary circulation cells in river channel confluence: measurement artifacts or coherent flow structures? Hydrol Process 14:2047–2071
81. Lane S, Parsons D, Best J, Orfeo O, Kostaschunk R, Hardy R (2008) Causes of rapid mixing at a junction of two large rivers: Rio Parana and Rio Paraguay. Argentina. Journal of Geophysical Research 113:F02019
82. Laraque A, Guyot JL, Filizola N (2009) Mixing processes in the Amazon River at the confluences of the Negro and Solimões Rivers, Encontro das Aguas, Manaus, Brazil. Hydrol Process 23:3131–3140
83. Lawal MA, Omosanya KOL (2023) Multidecadal changes in planform morphology of the confluence of River Niger and River Benue, West Africa. J Hydrol 623:129764
84. Leite Ribeiro M, Blanckaert K, Roy AG, Schleiss AJ (2012) Flow and sediment dynamics in channel confluences. J Geophys Res 117:F01035. https://doi.org/10.1029/2011JF002171
85. Leli IT, Stevaux JC, Bennert A, dos Santos VC, Luz LD (2023) Morphological resilience at the confluence of a very low discharge creek and a large river (upper Parana, Brazil). J S Am Earth Sci 123:104222. https://doi.org/10.1016/j.jsames.2023.104222
86. Lewis QW, Rhoads BL (2015) Rates and patterns of thermal mixing at a small stream confluence under variable incoming flow conditions. Hydrol Process 29(20):4442–4456
87. Lewis QW, Rhoads BL (2018) LSPIV measurements of two-dimensional flow structure in streams using small unmanned aerial systems: 1. Accuracy assessment based on comparison with stationary camera platforms and in-stream velocity measurements. Water Resour Res 54:8000–8018. https://doi.org/10.1029/2018WR022550
88. Lewis QW, Rhoads BL (2018) LSPIV measurements of two-dimensional flow structure in streams using small unmanned aerial systems: 2 Hydrodynamic mapping at river confluences. Water Resources Research. https://doi.org/10.1029/2018WR022551
89. Lewis Q, Rhoads B, Sukhodolov A, Constantinescu G (2020) Advective lateral transport of streamwise momentum governs mixing at small river confluences. Water Resources Research. https://doi.org/10.1029/2019WR026817
90. Li. K., Yuan, S., Tang., H., Xiao, Y., Gualtieri, C. (2019). Preliminary analysis of hydrodynamics and water chemistry at the confluence of Yangtze River and Poyang Lake, China. *XXXVIII IAHR Congress*, Panama City. Panama, September, 1/6, 2019
91. Li K, Tang H, Yuan S, Xiao Y, Xu L, Huang S, Rennie CD, Gualtieri C (2022) A field study of near-junction-apex flow at a large river confluence and its response to the effects of floodplain flow. J Hydrol 610:127983. https://doi.org/10.1016/j.jhydrol.2022.127983
92. Li K, Tang H, Yuan S, Xu L, Xiao Y, Gualtieri C (2022) Temporal variations of sediment and morphological characteristics at a large confluence accounting for the effects of floodplain submergence. Int J Sedim Res 37(5):619–638. https://doi.org/10.1016/j.ijsrc.2022.04.004
93. Lingman M, Lund J, Fürth M (2024) A comprehensive review of hydrodynamic studies on fish schooling. Bioinspir Biomim 19:011002
94. Liu X, Tong X, Yang T, Mohapatra S, Hua Z, Zhang Y, Chu K, Xue H (2023) Insights into effects of discharge ratio on flow characteristics and pollutant transport in a Y-shaped open channel confluence with emergent rigid vegetation. J Environ Manage 332:117421. https://doi.org/10.1016/j.jenvman.2023.117421
95. Luis SM, Pasternack GB (2023) Local hydraulics influence habitat selection and swimming behavior in adult California Central Valley Chinook salmon at a large river confluence. Fish Res 261:106634. https://doi.org/10.1016/j.fishres.2023.106634
96. Luz, L.D., Szupiany, R.N., Parolin, M., Silva, A., Stevaux, J.C. (2020). Obtuse-angle vs. confluent sharp meander bends: insights from the Paraguay-Cuiabá confluence in the tropical Pantanal wetlands Brazil. *Geomorphology*. https://doi.org/10.1016/j.geomorph.2019.106907
97. Lyubimova T, Lepikhin A, Ya P, Konovalov V, Tiunov A (2014) Formation of the density currents in the zone of confluence of two rivers. J Hydrol 508:328–342
98. Lyubimova TP, Lepikhin AP, Parshakova YN, Kolchanov VY, Gualtieri C, Roux B, Lane SN (2020) A Numerical Study of the Influence of Channel-Scale Secondary Circulation on Mixing Processes Downstream of River Junctions. Water 12(11):2969. https://doi.org/10.3390/w12112969
99. Lyubimova TP, Lepikhin AP, Parshakova YN, Kolchanov VY, Gualtieri C, Lane S, Roux B (2021) Hydrodynamic aspects of confluence of rivers with different water densities. J Appl Mech Tech Phys 62(7):1211–1221

100. Mackay JR (1970) Lateral mixing of the Liard and Mackenzie rivers downstream form their confluence. Can J Earth Sci 7(1):111–124
101. Marinho T, Filizola N, Martinez J-M, Armijos E, Nascimento A (2018) Suspended Sediment Variability at the Solimões and Negro Confluence between May 2013 and February 2014. Geosciences 8:265. https://doi.org/10.3390/geosciences8070265
102. Marinho T, Furtado A, Dos Santos V, Zumak A, Nascimento A, Filizola N (2022) Riverbed morphology and hydrodynamics in the confluence of complex mega rivers - A study in the Branco and Negro rivers, Amazon basin. J S Am Earth Sci 118:103969
103. Martin AR, Da Silva VME, Salmon DL (2004) Riverine habitat preferences of Botos (Inia geoffrensis) and Tucuxis (Sotalia fluviatilis) in the Central Amazon. Mar Mamm Sci 20(2):189–200
104. Martone, I., Gualtieri, C., Endreny, T.A. (2019). Analysing the effect of confluence hydrodynamics and morphodynamics on hyporheic fluxes. A field study in two small streams. *XXXVIII IAHR Congress*, Panama City, Panama, September 1/6, 2019
105. Martone I, Gualtieri C, Endreny TA (2020) Characterization of Hyporheic Exchange Drivers and Patterns within a Low-Gradient, First-Order, River Confluence during Low and High Flow. Water 12:649. https://doi.org/10.3390/w12030649
106. Martone I, Gualtieri C, Endreny TA (2022) Field Study Analysis of Temporal Temperature Methods to Estimate Hyporheic Fluxes within a Natural River Confluence Using VFLUX2. Environmental Science Proceedings 21:71. https://doi.org/10.3390/environsciproc2022021071
107. McClain ME, Boyer EW, Dent CL, Gergel SE, Grimm NB, Groffma PM, Pinay G (2003) Biogeochemical Hot Spots and Hot Moments at the Interface of Terrestrial and Aquatic Ecosystems. Ecosystems 6(4):301–312
108. Mohsen A, Kovács F, Mezősi G, Kiss T (2021) Sediment Transport Dynamism in the Confluence Area of Two Rivers Transporting Mainly Suspended Sediment Based on Sentinel-2 Satellite Images. Water 13:3132. https://doi.org/10.3390/w13213132
109. Mosley MP (1976) An experimental study of channel confluences. J Geol 84(5):535–562. https://doi.org/10.1086/628230
110. Mriganka, M., Saikat, D. (2023). Assessment of Changes in Brahmaputra River Course at the Pagladia Confluence Point using Remote Sensing and GIS Techniques, *Disaster Advances*, 16, November 2023
111. Nakajima R, Rimachi EV, Santos-Silva EN, Calixto LSF, Leite RG, Khen A, Yamane T, Mazeroll AI, Inuma JC, Utumi EYK, Tanaka A (2017) The density and biomass of mesozooplankton and ichthyoplankton in the Negro and the Amazon Rivers during the rainy season: the ecological importance of the confluence boundary. PeerJ 5:e3308
112. Nikora V (2010) Hydrodynamics of aquatic ecosystems: an interface between ecology, biomechanics and enviromental fluid mechanics, *River Research and Applications*, 26, 367–384Paola, C. (1997). When streams collide Nature 387:232–233
113. Pandey AK, Mohapatra PK (2023) Flow Dynamics and Pollutant Transport at an Artificial Right-Angled Open-Channel Junction with a Deformed Bed. J Hydraul Eng 149(4):04023006
114. Park E, Latrubesse EM (2015) Surface water types and sediment distribution patterns at the confluence of mega rivers: The Solimões-Amazon and Negro Rivers junction. Water Resour Res 51:6197–6213
115. Parsons DR, Best JL, Lane SN, Orfeo O, Hardy RJ, Kostaschuk R (2007) Form roughness and the absence of secondary flow in a large confluence–diffluence, Rio Paraná, Argentina. Earth Surf Proc Land 32:155–162. https://doi.org/10.1002/esp.1457
116. Piégay H, Arnaud F, Belletti B, Bertrand M, Bizzi S, Carbonneau P, Dufour S, Liébault F, Ruiz-Villanueva V, Slater L (2020) Remotely sensed rivers in the Anthropocene: state of the art and prospects. Earth Surf Proc Land 45:157–188. https://doi.org/10.1002/esp.4787
117. Pouchoulin S, Le Coz J, Mignot E, Gond L, Riviere N (2020) Predicting transverse mixing efficiency downstream of a river confluence. Water Resources Research. https://doi.org/10.1029/2019WR026367
118. Prats J, Armengol J, Marcé R, Sánchez-Juny M, Dolz J (2010) Dams and reservoirs in the lower Ebro River and its effects on the river thermal cycle. Handbook of Environmental Chemistry 13:77–95
119. Proust S, Berni C, Nikora V (2022) Shallow mixing layers over hydraulically smooth bottom in a tilted open channel. J Fluid Mech 951:A17
120. Power ME, Dietrich WE (2002) Food webs in river networks. Ecol Res 17(4):451–471
121. Raj, C., Singh, V. (2023). Study of Morphological Changes of River Ganga at the Confluence of River Kosi. In: Timbadiya, P.V., Patel, P.L., Singh, V.P., Barman, B. (eds) Fluid Mechanics and Hydraulics. HYDRO 2021. *Lecture Notes in Civil Engineering*, vol 314. Springer, Singapore. https://doi.org/10.1007/978-981-19-9151-6_22

122. Ramòn CL, Hoyer AB, Armengol J, Dolz J, Rueda FJ (2013) Mixing and circulation at the confluence of two rivers entering a meandering reservoir. Water Resour Res 49(3):1429–1445
123. Ramòn CL, Armengol J, Dolz J, Prats J, Rueda FJ (2014) Mixing dynamics at the confluence of two large rivers undergoing weak density variations. Journal of Geophysical Research: Oceans 119(4):2386–2402
124. Ramòn CL, Prats J, Rueda FJ (2016) The influence of flow inertia, buoyancy, wind, and flow unsteadiness on mixing at the asymmetrical confluence of two large rivers. J Hydrol 539:11–26
125. Rathbun RE, Rostad CE (2004) Lateral mixing in the Mississippi River below the confluence with the Ohio River. Water Resour Res 40:W05207. https://doi.org/10.1029/2003WR002381
126. Rhoads BL (1987) Changes in stream characteristics at tributary junctions. Phys Geogr 8:346–361
127. Rhoads BL, Kenworthy ST (1995) Flow structure at an asymmetrical stream confluence. Geomorphology 11(4):273–293. https://doi.org/10.1016/0169-555X(94)00069-4
128. Rhoads BL, Kenworthy ST (1998) Time-averaged flow structure in the central region of a stream confluence. Earth Surface Processes and Landforms: The Journal of the British Geomorphological Group 23(2):171–191
129. Rhoads BL, Sukhodolov AN (2001) Field investigation of three-dimensional flow structure at stream confluences: 1. Thermal mixing and time-averaged velocities, Water Resources Research 37(9):2393–2410
130. Rhoads BL, Sukhodolov AN (2004) Spatial and temporal structure of shear layer turbulence at a stream confluence. Water Resour Res 40(6):W06304. https://doi.org/10.1029/2003WR002811
131. Rhoads BL, Sukhodolov AN (2008) Lateral momentum flux and the spatial evolution of flow within a confluence mixing interface. Water Resour Res 44(8):W08440. https://doi.org/10.1029/2007WR006634
132. Rhoads BL, Riley JD, Mayer DR (2009) Response of bed morphology and bed material texture to hydrological conditions at an asymmetrical stream confluence. Geomorphology 109(3–4):161–173. https://doi.org/10.1016/j.geomorph.2009.02.029
133. Rice SP, Ferguson RI, Hoey TB (2006) Tributary control of physical heterogeneity and biological diversity at river confluences. Can J Fish Aquat Sci 63(11):2553–2566
134. Rice, S.P., Kiffney, P., Greene, C., Pess, G.R. (2008). The ecological importance of tributaries and confluences, River Confluences, Tributaries and the Fluvial Network, edited by S.P. Rice, A.G. Roy and B. Rhoads, 17–32, Wiley & Sons, Chichester
135. Riley JD, Rhoads B, Parsons DR, Johnson KK (2014) Influence of junction angle on three-dimensional flow structure and bed morphology at confluent meander bends during different hydrological conditions. Earth Surf Proc Land 40:252–271
136. Rodi, W, Constantinescu, G., Stoesser, T. (2013). Large Eddy Simulation in hydraulics IAHR Monograph, CRC Press, Taylor & Francis Group (ISBN-10: 1138000247)
137. Roy A, Rhoads B, Rice S (2008). River confluences, tributaries and the fluvial network. https://doi.org/10.1002/9780470760383
138. Sabrina S, Lewis Q, Rhoads BL (2021) Large-scale particle image velocimetry reveals pulsing of incoming flow at a stream confluence. Water Resources Research. https://doi.org/10.1029/2021WR029662
139. Sambrook Smith G, Nicholas AP, Best JL, Bull JM, Dixon SJ, Goodbred S, Sarker MH, Vardy ME (2019) The sedimentology of river confluences. Sedimentology 66:391–407
140. Shen X, Li R, Huang J, Feng J, Hodges B, Li K, Xu W (2016) Shelter construction for fish at the confluence of a river to avoid the effects of total dissolved gas supersaturation. Ecol Eng 97:642–648. https://doi.org/10.1016/j.ecoleng.2016.10.055
141. Shen X, Hodges B, Li R, Li Z, Fan J, Cui N, Cai H (2021) Factors Influencing Distribution Characteristics of Total Dissolved Gas Supersaturation at Confluences. Water Resources Research. https://doi.org/10.1029/2020WR028760
142. Shen X, Li R, Cai H, Feng J, Wan H (2022) Characteristics of secondary flow and separation zone with different junction angle and flow ratio at river confluences. J Hydrol 614:128537. https://doi.org/10.1016/j.jhydrol.2022.128537
143. Shen X, Li S, Sun S, Qing D, Li D, Wang K, Gao W, Cao L (2023) The mechanism of dissolved oxygen mixing and atmospheric reoxygenation at the confluence with different flow ratios and junction angles. Journal of Hydrology. https://doi.org/10.1016/j.jhydrol.2023.130191
144. Shi L, Sun J, Lin B, Liu Z, Zuo X (2022) Hydro-thermodynamic processes at a large confluence under reservoir regulation. Water Resources Research. https://doi.org/10.1029/2022WR033315
145. Song J, Zhang G, Wang W, Liu Q, Jiang W, Guo W, Tang B, Bai H, Dou X (2017) Variability in the vertical hyporheic water exchange affected by hydraulic conductivity and river morphology at a natural confluent meander bend. Hydrol Process 31:3407–3420

146. Sukhodolov AN, Rhoads BL (2001) Field investigation of three-dimensional flow structure at stream confluences: 2. Turbulence Water Resources Research 37(9):2411–2424. https://doi.org/10.1029/2001WR000317
147. Sukhodolov A, Krick J, Sukhodolova T, Cheng Z, Rhoads B, Constantinescu G (2017) Turbulent flow structure at a discordant river confluence: Asymmetric jet dynamics with implications for channel morphology. J Geophysical Research: Earth Surface 122:1278–1293. https://doi.org/10.1002/2016JF004126
148. Sukhodolov AN, Sukhodolova TA (2019) Dynamics of flow at concordant gravel bed river confluences: Effects of junction angle and momentum flux ratio. J Geophys Res Earth Surf 124(2):588–615. https://doi.org/10.1029/2018JF004648
149. Sukhodolov AN, Shumilova OO, Constantinescu GS, Lewis QW, Rhoads BL (2023) Mixing dynamics at river confluences governed by intermodal behavior. Nat Geosci 16:89–93. https://doi.org/10.1038/s41561-022-01091-1
150. Szupiany RN, Amsler ML, Parsons DR (2009) Morphology, flow structure, and suspended bed sediment transport at two large braid-bar confluences. Water Resources Research. https://doi.org/10.1029/2008WR007428
151. Szupiany R.N., Garcia C.M., Oberg K. (2017). Acoustic Instruments for Mean Flow characterization in field conditions. Acoustic Doppler Current Profilers (ADCP), Section 3.3 in Experimental Hydraulics, Volume II; J. Aberle, C.D. Rennie, D.M. Admiraal, M. Muste (Editors); Taylor & Francis, New York, NY
152. Tang H, Zhang H, Yuan S (2018) Hydrodynamics and contaminant transport on a degraded bed at a 90-degree channel confluence. Environ Fluid Mech 18(2):443–463. https://doi.org/10.1007/s10652-017-9562-8
153. Tang H, Yuan S, Li Z, Cao H, Jiang C, Gualtieri C (2023) Hydrodynamics and sediment transport in Poyang Lake under the effects of wind and backflow. Hydrology Research. https://doi.org/10.2166/nh.2023.191
154. Trevethan M, Martinelli A, Oliveira M, Ianniruberto M, Gualtieri C (2015) Fluid dynamics sediment transport and mixing about the confluence of Negro and Solimões rivers Manaus Brazil, *36th IAHR World Congress*. The Netherlands, The Hague, p 80094
155. Trevethan M, Ventura Santos R, Ianniruberto M, Santos A, De Oliveira M, Gualtieri C (2016) Influence of tributary water chemistry on hydrodynamics and fish biogeography about the confluence of Negro and Solimões rivers Brazil, *11th International Symposium on EcoHydraulics (ISE 2016)*. Melbourne, Australia, p 25674
156. Trinci G, Harvey GL, Henshaw AJ, Bertoldi W, Hölker F (2017) Life in turbulent flows: interactions between hydrodynamics and aquatic organisms in rivers. WIREs Water 4:e1213. https://doi.org/10.1002/wat2.1213
157. Umar M, Rhoads B, Greenberg JA (2018) Use of multispectral satellite remote sensing to assess mixing of suspended sediment downstream of large river confluences. J Hydrol 556:325–338. https://doi.org/10.1016/j.jhydrol.2017.11.02
158. van Rooijen E, Mosselman E, Sloff K, Uijttewaal W (2020) The effect of small density differences at river confluences. Water 12(11):3084
159. Wang Z, Xia J, Zhou M, Li T (2019) Numerical modeling of hyperconcentrated confluent floods from the Middle Yellow and Lower Weihe Rivers. Water Resour Res 55:1972–1987. https://doi.org/10.1029/2018WR024152
160. Wang X, Yang J, Wang F, Xu N, Li P, Wang A (2023) Numerical modeling of the dispersion characteristics of pollutants in the confluence area of an asymmetrical river. Water 15:3766. https://doi.org/10.3390/w15213766
161. Xie Q, Yang J, Lundström S, Dai W (2018) Understanding morphodynamic changes of a tidal river confluence through field measurements and numerical modeling. Water 10:1424. https://doi.org/10.3390/w10101424
162. Xu L, Yuan S, Tang H, Qiu J, Xiao Y, Whittaker C, Gualtieri C (2022) Mixing dynamics at the large confluence between the Yangtze River and Poyang Lake. Wat Resources Res. https://doi.org/10.1029/2022WR032195
163. Yang Q, Wang Y, Lu W, Wang X (2009) Experimental study on characteristics of separation zone in confluence zones in rivers. J Hydrol Eng 14(2):166–171. https://doi.org/10.1061/(ASCE)1084-0699(2009)14:2(166)
164. Yang H, Cong P (2019) Confluence dynamics in a modelled large sand-bed braided river. Water 11:1829. https://doi.org/10.3390/w11091829

165. Yu Q, Yuan S, Rennie CD (2020) Experiments on the morphodynamics of open channel confluences: Implications for the accumulation of contaminated sediments. J Geophys Res: Earth Surface. https://doi.org/10.1029/2019JF005438
166. Yuan S, Tang H, Xiao Y, Qiu X, Zhang H, Yu D (2016) Turbulent flow structure at a 90-degree open channel confluence: Accounting for the distortion of the shear layer. J Hydro-environ Res 12:130–147. https://doi.org/10.1016/j.jher.2016.05.006
167. Yuan S, Tang H, Xiao Y, Qiu X, Xia Y (2018) Water flow and sediment transport at open-channel confluences: An experimental study. J Hydraul Res 56:333–350. https://doi.org/10.1080/00221686.2017.1354932
168. Yuan S, Tang H, Xiao Y, Xia Y, Melching C, Li Z (2019) Phosphorus contamination of the surface sediment at a river confluence. J Hydrol 573:568–580. https://doi.org/10.1016/j.jhydrol.2019.02.036
169. Yuan S, Tang H, Li K, Xu L, Xiao Y, Gualtieri C, Rennie C, Melville B (2021) Hydrodynamics, sediment transport and morphological features at the confluence between the Yangtze River and the Poyang Lake. Wat Resources Res. https://doi.org/10.1029/2020WR028284
170. Yuan S, Xu L, Tang H, Xiao Y, Gualtieri C (2022) The dynamics of river confluences and their effects on the ecology of aquatic environment: a review. J Hydrodyn 34:1–14. https://doi.org/10.1007/s42241-022-0001-z
171. Yuan S, Zhu Y, Tang H, Xu L, Li K, Xiao Y, Gualtieri C (2022) Planform evolution and hydrodynamics near the multi-channel confluence between the Yarlung Zangbo River and the delta of the Niyang River. Geomorphology 402:108157. https://doi.org/10.1016/j.geomorph.2022.108157
172. Yuan S, Xu L, Tang H, Yang X, Whittaker C (2022) Swimming behavior of juvenile silver carp near the separation zone of a channel confluence. Int J Sediment Res. https://doi.org/10.1016/j.ijsrc.2021.08.002
173. Yuan S, Qiu J, Tang H, Xu L, Xiao Y, Liu M, Rennie C, Gualtieri C (2023) Fish community traits near a large confluence: Implications for its nodal effects in the river ecosystem. J Hydrol 626:130335
174. Yuan S, Yan G, Tang H, Xiao Y, Rahimi H, Aye N, Gualtieri C (2023) Effects of tributary floodplain on confluence hydrodynamics. J Hydraul Res 61(4):552–572. https://doi.org/10.1080/00221686.2023.2231413
175. Yuan S, Lin H, Tang H, Qiu J, Li Z, Luo X, Gualtieri C (2024) An optimized entropy-based model for estimating river confluence hydrodynamics: accounting for the effects of velocity dip. J Hydrol 628:130408
176. Yuan S, Zheng Y, Tang H, Chen Y, Xu L, Whittaker C, Gualtieri C (2024) Large wood transport and accumulation near the separation zone of a channel confluence. Wat Resources Res. https://doi.org/10.1029/2023WR034790
177. Yuan S, Lin J, Tang H, Zhu Y, Ran Q, Constantinescu G, Gualtieri C (2024) Near-surface turbulent dissipation at a laboratory-scale confluence: implications on gas transfer. Environ Fluid Mech. https://doi.org/10.1007/s10652-023-09964-8
178. Zeng J, Constantinescu G, Weber L (2008) A 3D non-hydrostatic model to predict flow and sediment transport in loose-bed channel bends. J Hydraul Res 46(3):356–372. https://doi.org/10.3826/jhr.2008.3328
179. Zeng J, Constantinescu G, Weber L (2010) 3D calculations of equilibrium conditions in loose-bed open channels with significant suspended sediment load. J Hydraul Eng. https://doi.org/10.1061/(ASCE)HY.1943-7900.0000213
180. Zhang Y, Wang P, Wu B, Hou S (2015) An experimental study of fluvial processes at asymmetrical river confluences with hyperconcentrated tributary flows. Geomorphology 230:26–36. https://doi.org/10.1016/j.geomorph.2014.11.001
181. Zhang T, Feng M, Chen K (2020) Hydrodynamic characteristics and channel morphodynamics at a large asymmetrical confluence with a high sediment-load main channel. Geomorphology 356:107066